University of Seville
Master in Nuclear Physics 2020/2021

Investigation of the separatrix ion temperature using impurity Charge Exchange Recombination Spectroscopy

Kiera McKay

Supervisor:
Eleonora Viezzer

Departamento de Física Atómica, Molecular y Nuclear
Facultad de Física

Plasma Science and Fusion Technology
Centro Nacional de Acceleradores

Abstract

The ion temperature of a magnetically confined plasma plays an important roll in that plasma's ability to initiate and sustain fusion reactions. In the development of fusion technology it is thus critical to be able to accurately characterize the ion temperature profile of a plasma. This work measured ion temperature using Charge Exchange Recombination Spectroscopy (CXRS). This method can involve injecting neutral molecules into the plasma, which can contaminate the ion spectral emissions with molecular line emissions, leading to inaccurate temperature measurements.

In this master thesis, a multi-gaussian fit was designed to identify and subtract the molecular lines from the complex spectra detected by CXRS diagnostics at the ASDEX Upgrade tokamak for three discharges in different energy confinement modes (H-mode. L-mode, and I-mode). Impurity temperature and intensity profiles were determined for the three discharges using measurements at the edge of the plasma and in the Scrape-Off layer, as these regions were most likely to be affected by the injected neutral molecules. The results suggest that molecular lines effect measurements for a larger range of radial points in the case of L-mode and I-mode discharges, while the H-mode discharge showed a greater difference in temperature magnitude after subtracting molecular contributions, but in a smaller radial range.

1D kinetic simulations were performed to model the density profile of the molecular neutral. Molecular neutrals were found to penetrate the farthest into the plasma in L-mode, followed by I-mode, with H-mode showing the least penetration.

Contents

1 Introduction

1.1 Motivation

Humans have long used their incredible mental faculty to build innovative tools meant to control and improve their environment, and in doing so have clearly marked their presence on the planet earth. However, after taking advantage of the earth for so long, the evidence that human action has steadily been destroying the environment is unavoidable and can only lead to one pressing conclusion: it is our desperate responsibility to turn our minds towards creating technology meant to protect and replenish the planet that is our home, ensuring a safe future for the next generations. A crucial step in our process to slow the progress of climate change is developing renewable energy sources to replace our dependence on fossil fuels. One such promising energy source currently in development is fusion, a nuclear process in which light atoms fuse together while releasing energy. Fusion reactions are only possible in plasmas, a state of matter in which a gas has been heated to the point of ionization. However a plasma's fusion capabilities vary, and are impacted most strongly by three defining qualities: temperature (T), confinement time (τ_e), and particle density (n). Increasing the energy of the particles, the time in which they are kept in a plasma state, and the proximity of the particles to one another results in increased likelihood that the particles will undergo fusion. The relation between these three factors that must be achieved in order to reach ignition, the state in which the energy production of the fusion reactions outpace the cooling mechanisms, is defined by the Lawson criterion:

$$n \cdot T \cdot \tau_e > 5 \cdot 10^{21} m^{-3} \cdot keV \cdot s^1 \tag{1}$$

Since optimizing these three qualities is crucial to inducing a sustained fusion

[1] Temperatures are expressed as energies

burn, it is of great importance to develop diagnostics and analytical techniques that allow scientists to measure them accurately. This master thesis will specifically focus on determining the ion temperature from spectral measurements taken at the edge of the plasma, applying a multi-gaussian spectrum fitting technique developed in [1]. The edge of the plasma is a region where such temperature measurements become complex, yet it is a critical region to study due to its proximity to the walls of the plasma confinement device. Furthermore, the conditions at the edge of the plasma define the boundary conditions of the core of the plasma where the majority of fusion reactions occur, thus the state of the edge impacts the overall energy capabilities of the plasma. This master thesis will compare fitting accuracy for three different confinement states.

1.2 Nuclear Fusion

Fusion, the nuclear process that powers the sun and stars, consists of the fusing of two light atoms into a heavier atom. The binding energy per nucleon, shown in Figure 1, varies with atomic number and peaks at A=56, indicating nuclei around this atomic number are most tightly bound. This peak reveals two possible ways of releasing nuclear energy: by breaking apart heavier atoms of $A > 56$ to release energy in a fission reaction, a process that powers all current nuclear power plants, or by combining the lighter elements for a fusion reaction. In the formation of the heavier atom during a fusion reaction, some of the mass of the original atoms is converted into energy in accordance with the mass-energy equivalence stated in Einstein's special theory of relativity. The result is thus a more tightly bound atom with a mass less than the sum of the initial atoms and a release of excess energy that can be collected and repurposed as a renewable energy source. Notably, the binding energy curve has a very steep increase at low A, indicating that more energy is available in a fusion

reaction than a fission reaction. There are several combinations of light atoms that can produce a fusion reaction, the most promising of which is between deuterium (D) and tritium (T), two isotopes of hydrogen, which combine to produce:

$$^2D +^3 T \rightarrow^4 He + n + 17.6MeV \tag{2}$$

D-T fusion is favorable due to its high cross-section and high energy yield as compared to other combinations. The materials required for this reaction are also readily accessible: deuterium is easily extracted from water, and tritium, while not naturally occurring on earth, can be synthesized from Lithium. The availability of the materials and the ease at which the byproducts can be safely disposed makes fusion an auspicious potential energy source. However, a sustained fusion burn, in which the output energy is greater than the input energy, has yet to be achieved on earth due to the complicated conditions required for such production. For a fusion reaction to occur, the particles must overcome the Coulomb force and thus must have high kinetic energies. This requires that the fusing materials have very high temperatures such that they exist in a plasma state. A plasma is a fourth state of matter in which a gas has been heated to the point of ionization, producing a quasineutral material that can be described by collective motion rather than localized particle collisions. Given that plasmas are composed entirely of charged particles, they are capable of conducting electricity well and can be penetrated and confined by magnetic fields, which are key components in the design of fusion reactors.

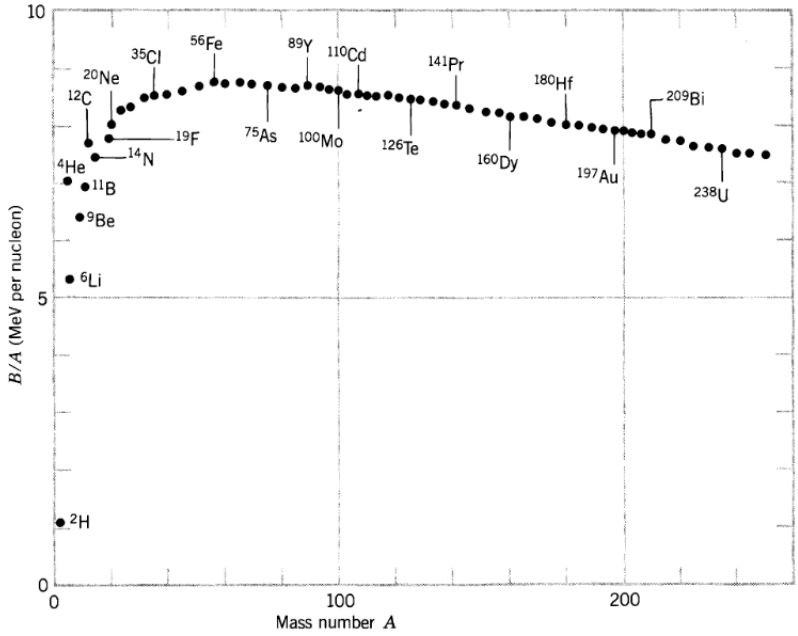

Figure 1: The binding energy per nucleon, taken from [2]

1.3 Magnetic Confinement in Tokamaks

One of the best performing plasma confinement devices is the tokamak. The tokamak utilizes the magnetic confinement method to contain a plasma within a torus shaped vacuum chamber. This requires the implementation of a layered magnetic field comprised of a poloidal and toroidal component. The toroidal magnetic field is produced by toroidal field coils that wrap around the tokamak, while the poloidal field is produced by inducing a plasma current using a transformer in the center of the tokamak. The plasma acts as a secondary coil to the central transformer, thus an electric field can be induced by varying the magnetic flux across the inner poloidal field coils. Plasma experiments in tokamaks, called discharges, are limited in their duration due to the dependence on a transformer for confinement, thus the maximum length of a discharge is determined by the characteristics of the transformer coil. The layered poloidal and toroidal fields result in helical magnetic field lines that contain the plasma while minimizing particle drift loses. The geometry of the field

lines results in nested magnetic flux surfaces that are toroidally independent.

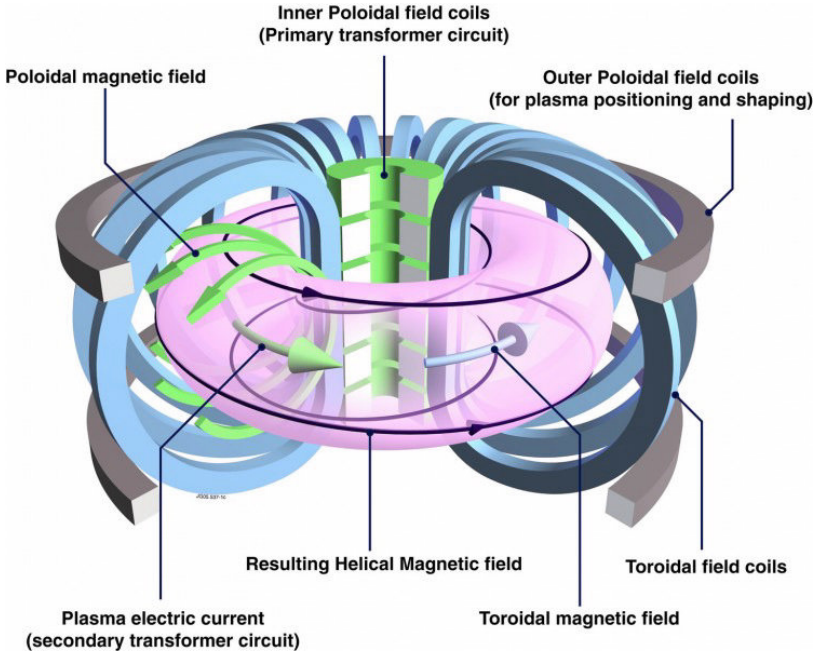

Figure 2: Diagram of a tokamak [3]

A schematic of a tokamak can be found in Figure 2, and a diagram of the nested flux surfaces can be found in Figure 3. It is common practice to describe a plasma using radial coordinates normalized to the magnetic flux surfaces, such that $\rho_{pol} = 0$ is at the center of the plasma and $\rho_{pol} = 1$ is at the last closed flux surface (LCFS), also referred to as the separatrix. This radial coordinate is defined as:

$$\rho_{pol} = \sqrt{\frac{\Psi - \Psi_0}{\Psi_S - \Psi_0}} \tag{3}$$

where Ψ is the poloidal flux, Ψ_0 is the poloidal flux at the magnetic axis, and Ψ_S is the poloidal flux at the separatrix. The region outside of the separatrix is called the Scrape-Off layer (SOL).

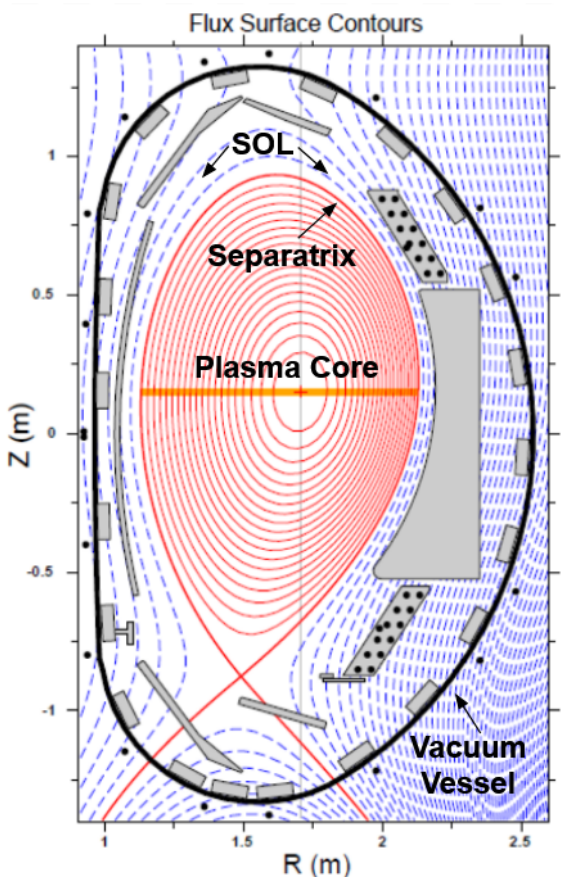

Figure 3: Magnetic flux surface contours in a bisection of the ASDEX Upgrade tokamak. Red lines indicate flux surfaces within the Last Closed Flux Surface (shown as the outermost red line), while dotted gray lines show flux outside the LCFS [4].

Beyond the challenges of confining the plasma, there is also the challenge of heating it, as plasmas must be heated to temperatures approaching tens of keV. There are two primary methods of heating utilized in tokamaks: Neutral Beam Injection (NBI) and Electromagnetic Wave heating. In Neutral Beam Injection, high energy neutral atoms are propelled into the plasma where they ionize and transfer their energy through collisions, heating the plasma. In Electromagnetic Wave heating, waves are emitted into the plasma at the resonance frequency of either the ions or the electrons, utilizing either Ion Cyclotron Resonance Heating (ICRH) or Electron Cyclotron Resonance Heating (ECRH) respectively. The species of choice is heated, and the particles

then transfer heat by colliding with the other species to ensure the plasma is heated throughout. Most of the input energy demands for fusion in tokamaks goes toward heating the plasma, however in a future fusion power plant the plasma would be self-sufficiently heated by the energized alpha particles that are created by the D-T reaction, allowing for a sustained burn with minimal external input.

1.4 Scope of this Master Thesis

Given the importance of ion temperature for a successful fusion reactor, as described by the Lawson Criteria, it is critical to have accurate methods of measuring ion temperature in all regions of the plasma. This master thesis seeks to contribute to improved temperature diagnostic processing by analyzing the molecular neutral contributions to impurity charge exchange recombination spectroscopy (CXRS) measurements. CXRS involves the detection of spectral emissions caused by charge exchange between neutrals and ions, however when the neutrals in the reaction are molecules, the molecular emissions of the neutrals can contaminate the ion spectral lines that are being studied. This master thesis will analyze CXRS impurity spectral data measured on the ASDEX Upgrade tokamak to measure the ion temperature in the edge and Scrape-Off Layer of the plasma. This analysis will involve the development of a multi-gaussian fit to characterize the effect of molecular neutral contamination on impurity spectra. The multi-gaussian analysis technique will be applied to three plasma discharges, all in different energy confinement modes, so as to compare the molecular contributions for a variety of plasma conditions. In the interest of evaluating the theoretical molecular contributions, this master thesis will also include Kinetic Neutral One Dimensional (KN1D) simulations to model the density distribution of both molecular and atomic neutrals for all three plasma discharges.

Chapter two will be comprised of theoretical background on particle motion and

the energy confinement modes studied in this thesis. Chapter three will discuss the experimental setup through which the CXRS measurements were produced, describing both ASDEX Upgrade and the Charge Exchange diagnostic. Chapter four outlines the analysis tools used to treat the experimental data, as well as the program used to simulate the neutral interactions and resulting density profiles. Chapter five will go into detail about the resulting experimental temperature profiles and simulated neutral density profiles, discussing the implications about molecular contributions to spectral measurements and the dependability of the ion temperature measurements. A final summary and conclusions will be presented in Chapter 6.

2 Theoretical Background

2.1 Particle Motion and Drifts

Given that a magnetically confined plasma is composed entirely of charged particles in an externally imposed magnetic field, the motion of the individual particles is complex. First we must consider the behavior of a single charged particle in a magnetic field without the presence of other charged particles. Such a particle would be affected by the lorentz force, given by:

$$\boldsymbol{F} = m\frac{d\boldsymbol{v}}{dt} = q\boldsymbol{v} \times \boldsymbol{B} \tag{4}$$

where m and $\boldsymbol{v}$ are the mass and velocity of a particle with electric charge q. By solving this equation for $v_{\parallel}$ and $v_{\perp}$, we find that for a constant value of $\boldsymbol{B}$, the particle will gyrate around the magnetic field line with a gyro-frequency (also known as the cyclotron frequency) of

$$\omega = \frac{|q|B}{m} \tag{5}$$

and a gyro-radius (also known as the Larmor radius) of

$$r_L = \frac{mv_{\perp}}{|q|B} \tag{6}$$

The magnetic field lines act as a guiding center for the gyrating particle as it moves with constant $v_{\parallel}$, creating a helical trajectory shown in Figure 4.

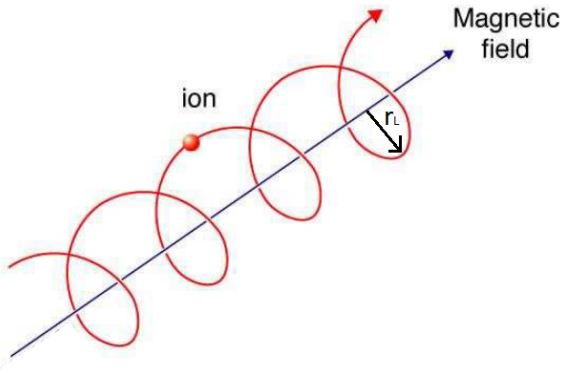

Figure 4: An ion gyrating around a magnetic field line [5]. The Larmor radius is designated by r_L.

Within a plasma, a particle will feel forces other than the Lorentz force, which will result in a particle drift when the force has a component perpendicular to the magnetic field. The presence of other forces will largely only affect the guiding center of the particles gyrating trajectory. The gyration itself can be considered independent from the drift under the conditions that the magnetic field has a large spatial gradient scale length ($\nabla B/B$) and a slow magnitude change with respect to time ($\frac{\partial B}{\partial t}/B$), as compared to the Larmor radius and cyclotron frequency. Generally, the drift velocity resulting from the presence of another force $\mathbf{F}$ can be describe as

$$\boldsymbol{B} = \frac{1}{q}\frac{\boldsymbol{F} \times \boldsymbol{B}}{B^2} \tag{7}$$

Within a tokamak, the three most important drifts are the $\mathbf{E} \times \mathbf{B}$ drift, the $\nabla \mathbf{B}$ drift, and the curvature drift. The first, $\mathbf{E} \times \mathbf{B}$ drift occurs due to the presence of an electric field perpendicular to the magnetic field. A particle of charge q placed in an electric field $\mathbf{E}$ will experience a force equal to $\mathbf{E}$q. Plugging this force in Equation 7 gives the drift velocity

$$\boldsymbol{v}_{\boldsymbol{E}\times\boldsymbol{B}} = \frac{\boldsymbol{E} \times \boldsymbol{B}}{B^2} \tag{8}$$

Notably, the charge of the particle cancels out, indicating that the drift velocity is the same for both ions and electrons. The second important drift, the $\nabla\mathbf{B}$ drift, is a result of the fact that the magnetic field applied in the tokamak is not constant along the major radius, but rather has a gradient along this axis. Another force perpendicular to the gradient and the magnetic field act on the particles, resulting in a drift expressed as

$$\boldsymbol{v}_{\nabla \boldsymbol{B}} = -\frac{mv_{\perp}^2}{2qB^3}\nabla \boldsymbol{B} \times \boldsymbol{B} \tag{9}$$

Here, the force is dependent on the mass of the particle and, unlike the $\mathbf{E} \times \mathbf{B}$ drift, the charge does not cancel, thus the $\nabla\mathbf{B}$ drift affects ions and electrons differently. Lastly, the particles experience a centrifugal force due to the fact that they travel along curved field lines, creating the curvature drift. The resulting velocity is

$$\boldsymbol{v}_{curv} = -\frac{mv_{\parallel}^2}{qB^3}\nabla \boldsymbol{B} \times \boldsymbol{B} \tag{10}$$

which takes a similar form to the $\nabla\mathbf{B}$ drift, except that it is determined by the parallel particle velocity rather than the perpendicular particle velocity.

2.2 Confinement Modes

It has been observed that the quality of the plasma confinement changes relative to the amount of power injected into the plasma, such that different confinement regimes with different characteristics can be defined.

2.2.1 L-mode

The first of these regimes to be discovered is the Low-Confinement mode (L-mode), which was the mode that all early tokamaks operated on. L-mode is characterized by large amounts of turbulence, which results in high energy leakage. In L-mode,

increasing the applied energy power results in decreased confinement below a certain threshold. Once this threshold is surpassed, the plasma rapidly transitions into the High-Confinement mode (H-mode).

2.2.2 H-mode

H-mode was first observed in 1982 on ASDEX, the precursor to the ASDEX Upgrade tokamak used for this study (discussed in Chapter 3.1) [6]. This regime, now the common operational scenario for most tokamaks, has increased plasma energy, increased ion density and decreased particle transport as compared to L-mode, causing energy confinement times to approximately double [7]. The most distinctive characteristic of an H-mode plasma is the development of a low turbulence region at the edge of the plasma called the Edge Transport Barrier (ETB). This region features a steep pressure gradient, which causes the plasma pressure profile to shift upward, creating a pedestal structure. This pressure pedestal structure coincides with the development of pedestal structures in the temperature and density profiles as well (see Figure 5). Given that high temperature and density are both necessary for a sustained fusion burn in accordance with the Lawson criteria (see Chapter 1), the H-mode regime seems very favorable to achieve ignition. The reduction to particle and heat transport perpendicular to the magnetic field caused by the ETB means that H-mode has much better confinement that L-mode.

2.2.3 Edge Localized Modes (ELMs)

When in H-mode, the plasma exhibits a periodic magnetohydrodynamic instability, referred to as Edge Localized Modes (ELMs). When these instabilities occur, particles and energy are expelled from the pedestal region of the plasma [9], [10], resulting in a decline in the pedestal structure of the density, temperature, and pressure profiles. This is unfavorable, both due to the breach in energy storage within the plasma

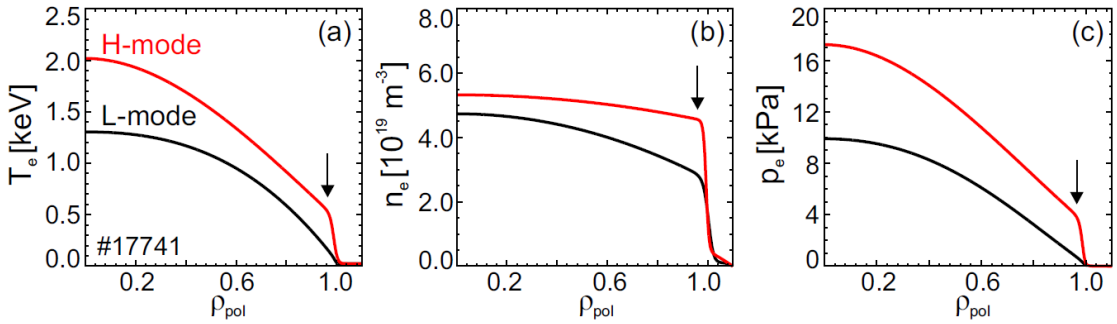

Figure 5: Comparison between H-mode and L-mode profiles. (a) shows the temperature profile, (b) shows the density profile, and (c) shows the pressure profile. H-mode shows steep gradients in the edge transport barrier region ($\rho_{pol} = 0.95 - 1.0$) for all three profiles, resulting in a pedestal structure. Taken from [8]

and the large heat flux the ELM applies to the walls of the tokamak. Although the physical mechanisms that cause ELMs are still largely unclear, they are an important phenomenon to study such that they can be mitigated or suppressed so as to prevent damage to the plasma facing components of the tokamak. Currently, the dominant theory suggests that ELMs are triggered to conserve the peeling-ballooning stability limit, where the peeling limit restricts the maximum edge plasma current and the ballooning limit restricts the edge pressure gradient [11], [12]. The ability to identify ELMs as they occur is necessary, both for studying the ELMs themselves and to factor them into analyses of other plasma phenomena. The divertor, an important instrument within a magnetic confinement device which allows for the removal of waste within the plasma such as impurities and ash (further discuss in Chapter 3.1), is useful for the detection of ELMs. When ELMs eject particles, they also eject impurities which are collected in the divertor. ELMs can thus be detected by noting spikes in the thermocurrent in the outer divertor caused by increased heat loads induced by the particle bursts.

2.2.4 I-mode

The Improved-Confinement mode, known as I-mode, is an alternative confinement regime that exhibits some favorable qualities from both L-mode and H-mode, specifically a lack of ELMs and improved energy confinement. I-mode plasmas have an edge transport barrier much like H-mode, however it only impedes heat transport while allowing for particle transport [13]. This results in a temperature pedestal structure similar to H-mode, but a particle density profile more reminiscent of L-mode. This temperature and density profile combination creates favorable conditions, such as a lack of large ELMs [14] and low impurity content and accumulation [15]. Both of these attributes help prevent energy leakage in the plasma, which motivates investigation into whether I-mode would be an advantageous regime for fusion reactors. In order for a plasma to enter I-mode, the power threshold of the transition from L-mode to H-mode must be kept high. This is typically done by employing unfavorable magnetic configurations such that the ∇B drift directs ions away from the X-point, a point where the poloidal field has zero magnitude [14]. As the plasma is heated, it progresses from L-mode to I-mode, then eventually to H-mode. The temperature and density profiles for L-mode, I-mode, and H-mode accessed by heating the plasma using NBI and ECRH are shown in Figures 6 and 7 [16]. For both heating methods, the I-mode temperature profile shows greater similarity to the the H-mode profile, while the I-mode density profiles shows greater similarity to the L-mode profile.

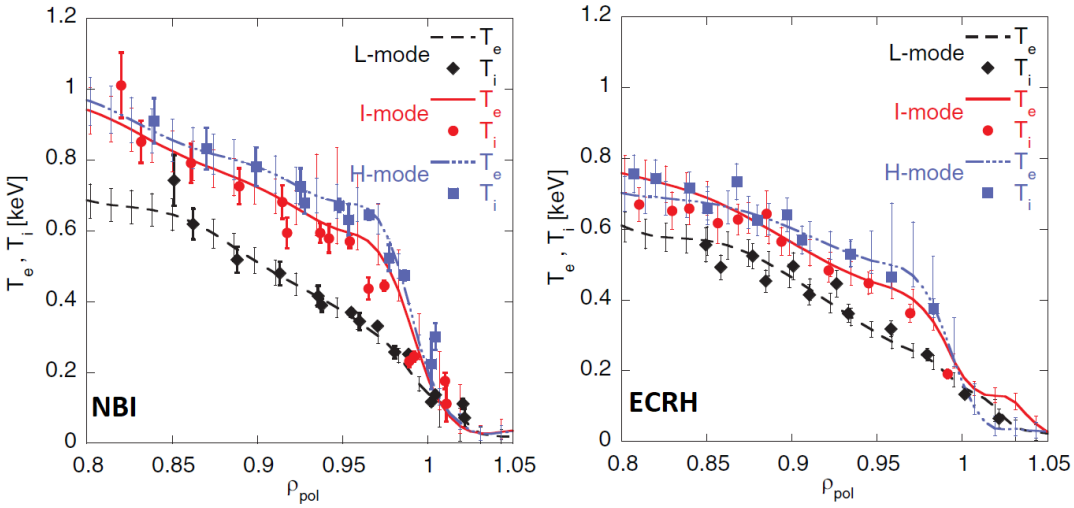

Figure 6: Ion and Electron temperature profiles for L-mode, I-mode, and H-mode plasmas. The different confinement modes were accessed using NBI heating (left) and ECRH (right). Taken from [16]

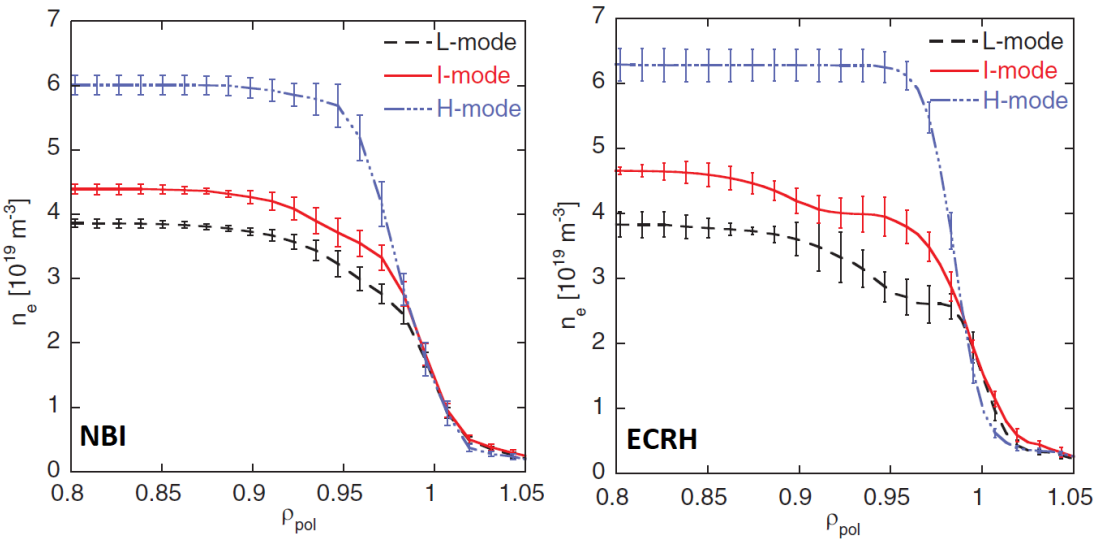

Figure 7: Electron density profiles for L-mode, I-mode, and H-mode plasmas. The different confinement modes were accessed using NBI heating (left) and ECRH (right). Taken from [16]

3 Experimental Setup

3.1 ASDEX Upgrade

The experimental measurements analyzed in this thesis were taken on the AxiSymmetric Divertor EXperiment (ASDEX) Upgrade (AUG) tokamak. AUG is a mid-size tokamak located at the Max-Planck Institute for Plasma Physics in Garching, Germany. The main characteristics of AUG are described in Table 1. AUG is notable for its magnetic field configuration that employs a divertor structure to handle impurity buildup. In this configuration, magnetic field lines outside of the LCFS direct escaped particles towards collector plates at the bottom of the vacuum chamber, referred to as the divertor, which acts to extract heat and ash (heavier ion impurities) created during fusion. This serves the dual purpose of protecting the walls of the plasma vessel from large thermal loads, while helping thermally insulate the plasma core to maintain high core temperatures.

The plasma facing wall tiles are made of tungsten, a unique material choice among existing tokamaks. Among the high-Z candidates for wall material, tungsten is a leading option due to its high melting point, low sputter erosion, and good thermomechanical properites, [17] qualities that suggest it is capable of high thermal loads.

The objective of AUG is to establish the physics of future tokamaks and fusion power plants, such as ITER and DEMO. Given that these projects are large scale, and thus incredibly demanding in terms of resources and time, it is critical that the physics for these projects be thoroughly investigated to ensure they are effective devices and to avoid damage to the machines. Accordingly, AUG experiments attempt to match the plasma conditions of projected fusion power plants.

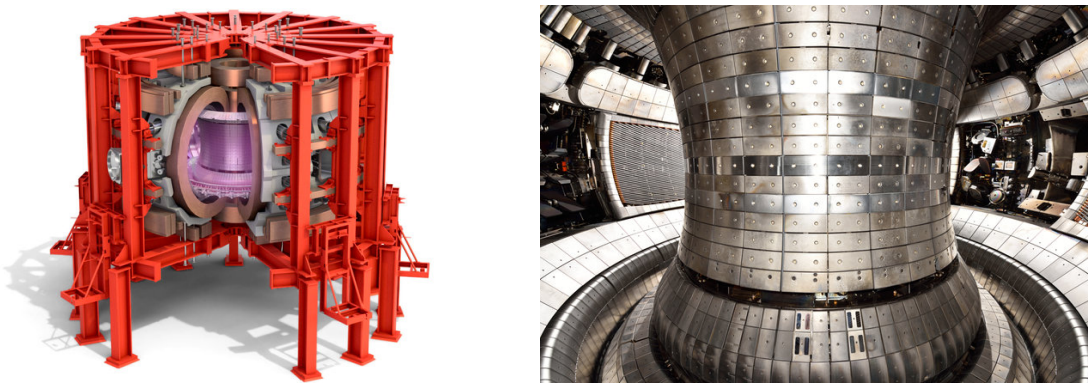

(a) (b)

Figure 8: Schematic of ASDEX Upgrade (left) and a photo taken of the inside of the plasma vessel at ASDEX Upgrade (right). The divot at the bottom of the vessel in the photo is the divertor. Images taken from [18], copyright IPP.

Major Radius (R_0)	1.65 m
Minor Plasma Radius (a)	0.5 m
Plasma Current (I_p)	0.4-1.2 MA
Toroidal Magnetic Field (B_{phi})	1.8-2.8 T
Maximum Heating Power (P_{heat})	30 MW
Plasma Species	D, H, He
Maximum Plasma Temperature	10^8 °C (8.6 keV)
Plasma Volume	14 m^3
Plasma Mass	3 mg
Electron Density	10^{20} m^{-3}

Table 1: Relevant characteristics and typical plasma parameters of AUG

3.2 Charge Exchange Recombination Spectroscopy

Charge eXchange Recombination Spectroscopy (CXRS) is a common diagnostic method used in tokamaks, used primarily to measure impurity properties [19]. This type of diagnostic takes advantage of the photon emitted in a charge exchange reaction between ions and neutrals. When a neutral particle interacts with a fully ionized impurity atom, charge is exchanged and the impurity atom enters an excited state. When the ion inevitably decays to the ground state, it emits a photon with a characteristic

wavelength that can then be captured by a spectrometer, producing a light spectrum that can be analyzed to reveal key information about the ion that emitted it. The processes is described as:

$$A^{Z+} + D \rightarrow A^{(Z-1)+*} + D^{+} \rightarrow A^{(Z-1)+} + D^{+} + h\nu \tag{11}$$

The resulting spectral lines can be fitted with Gaussian distributions (Figure 9). The temperature of the ions can then be derived from the Doppler width of the signal, the rotation can be derived from the Doppler shift, and the density can be derived from the signal intensity. Given that spectral lines are broadened due to the thermal motion of the emitting atoms, the impurity temperature can be calculated from the Full Width at Half Maximum (FWHM) of the Gaussian fit, which gives the relation:

$$T = \frac{mc^2}{8ln(2)\lambda_0^2 e^2} FWHM^2 \tag{12}$$

where m is the mass of the ion, c is the speed of light, λ_0 is the theoretical wavelength of the spectral line, and e is the charge of an electron. The wavelength where the spectral line peaks will not be equivalent to λ_0, but rather will be Doppler shifted an amount $\Delta\lambda$ due to the rotational velocity v_{rot} of the impurity, allowing for the calculation:

$$\frac{\Delta\lambda}{\lambda_0} = \frac{v_{rot} \cdot \boldsymbol{e}_{LOS}}{c} \tag{13}$$

where $\boldsymbol{e}_{LOS}$ is the unit vector along the line of sight (LOS) of the diagnostic. The LOS are the viewing lines defined by the optical head of the diagnostic. Noting where the LOS intersects with the path of the inserted neutrals allows for the localization of the charge exchange signal within the plasma.

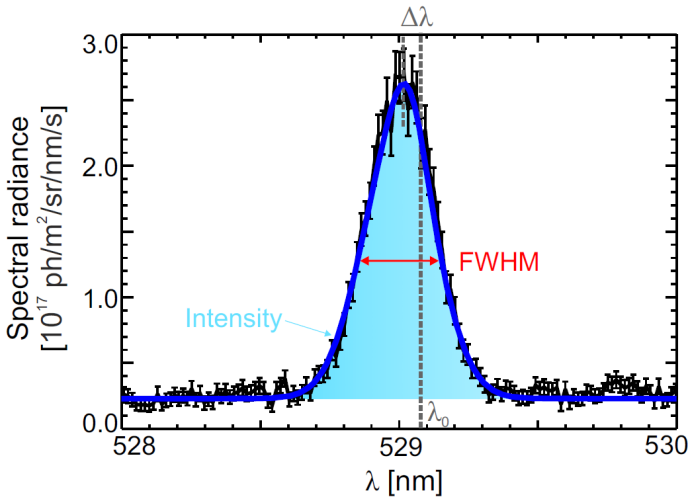

Figure 9: Example of a CXRS spectrum fitted with a Gaussian distribution. The temperature of the observed species can be determined from the Doppler width (FWHM), the rotational velocity can be determined from the Doppler shift ($\Delta\lambda$), and the density can be determined from the intensity. Taken from [8]

CXRS diagnostics typically utilize the Neutral Beam Injection (NBI) system used to heat the plasma to insert the neutrals necessary for the charge exchange reaction. However, since the NBI system is large and requires ample space for housing, it can only be used for CXRS measurements in the Low-field side (LFS) of the tokamak. The main alternative to the NBI system used for HFS CXRS measurements is a gas-puff based system [20]. This method utilizes a much more compact gas box to inject thermal neutrals to incite the charge exchange reaction. Notably, the neutrals from this system have about 0.025 eV, which is much lower energy than those injected by NBI, which range from 60-93 keV [21]. With much lower particle energy, the gas-puff particles cannot penetrate as far into the plasma. This means that Gas-Puff CXRS (GP CXRS) systems are only capable of producing measurements at the edge of the plasma. Experimentally it has been found that there is a geometric asymmetry in the distribution of impurities within the plasma, with greater density and accumulation at the High-Field side (HFS) than at the LFS [22, 23]. Accordingly, more intense signals

are expected from HFS measurements, which potentially leads to better plasma profile resolution [1].

The typical impurities measured on AUG are boron (B) and nitrogen (N). Generally, low Z impurities are favored for CXRS detection as they are more likely to be fully ionized throughout the plasma, while high Z impurities often are less abundant and may not be fully ionized throughout the whole plasma. This master thesis will utilize measurements made with the HFS gas-puff system on AUG (diagrammed in Figure 11), which was upgraded in 2019 and has both a poloidal and toroidal optical head [24]. The poloidal optical head has a spatial resolution that varies from 5-19 mm across the LOS, while the toroidal optical head has a spatial resolution of 10 mm. The spatial resolution denotes the range of uncertainty when determining the radial position of a detected spectral emission. The LOS are not point lines but rather cylindrical paths with a diameter of 5 mm, thus an emission detected by a given viewing window can only be localized within the 5 mm the LOS spans. The spatial resolution is further impacted by the angle at which the LOS crosses the injected neutral gas-puff. The effect of the angle of the LOS on the spatial resolution is illustrated in Figure 10. The poloidal optical head's LOS all cross the gas-puff at different angles, with the greatest angles and thus the poorest spatial resolution falls within the enclosed plasma, accounting for the range of spatial resolutions. Both diagnostics have 16 LOS that cover 7 cm of the HFS plasma edge. The systems have a temporal resolution of 4 ms. The neutral inserted by the gas puff valve is molecular D_2.

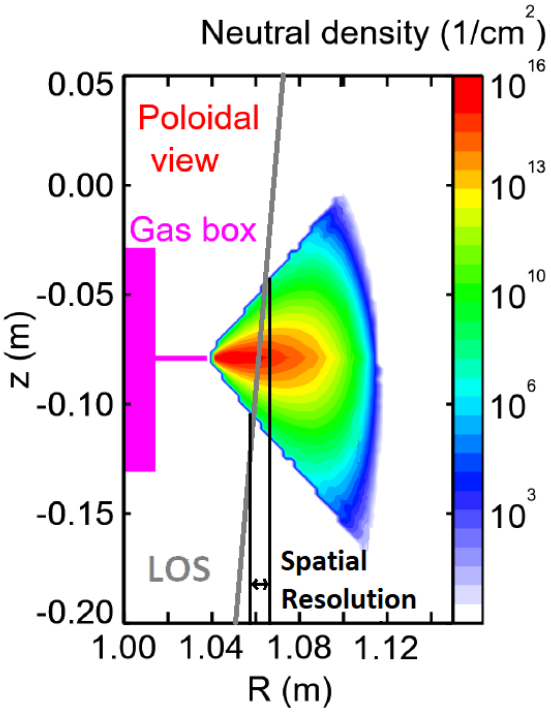

Figure 10: Geometry of LOS crossing the CXRS gas-puff. Spatial resolution is denoted as the distance between the two parallel black lines, accounting for angle and width of LOS. Illustration overlaid on gas-puff simulation discussed in [24]

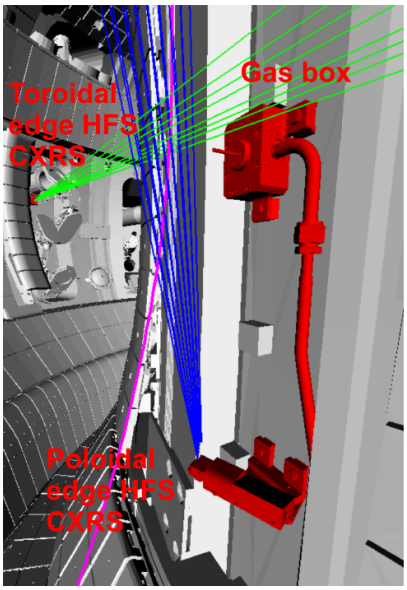

Figure 11: Schematic for the poloidal and toroidal CXRS HFS diagnostics and neutral emitting gas box inside the vacuum chamber of ASDEX Upgrade. Poloidal LOS shown in blue, Toroidal LOS shown in green. Taken from [24]

3.3 Electron temperature and density measurements

Although this work is primarily interested in ion measurements, electron measurements are important to have a more complete view of the plasma. Electron temperature (T_e) and density (n_e) profiles are used in this work to radially align the measured impurity profiles (discussed in the next section), and as input for the 1D kinetic simulations discussed in chapter 4.2. The two diagnostics used for this master thesis are the electron cyclotron emission (ECE) and the Thomson scattering (TS) diagnostics.

The ECE diagnostic measures electron radiation emissions to determine information about the electron temperature. It measures the emissions at the electron's angular cyclotron frequency $\omega_{c,e} = eB/m_e$ and its harmonics $\omega_{k,e} = k\omega_{c,e}$. The intensity of this frequency adheres to Planck's law of black body radiation, with the assumptions that the radiation and electron temperature are the same and that the electrons fall into a Maxwellian distribution. At high temperatures, the law of black body radiation gives the Rayleigh-Jeans expression:

$$I_\omega = \frac{\omega^2}{2\pi^2 c^2} k_B T_e \tag{14}$$

The radial position of the emitted radiation can be determined based on the variation of the toroidal magnetic field along the major radius, which has a 1/R relationship. Notably, the black-body assumption is only valid for optically thick regions of the plasma, which does not include the plasma edge due to its low density. Because of this, the ECE data is not used for determining T_e at the edge of the plasma. The ECE system at AUG has a spatial resolution of 1 cm and a temporal resolution of 1 μs [25, 26].

The TS diagnostic is used to determined both T_e and n_e by measuring the elastic scattering of an electromagnetic wave off of charged particles. Electromagnetic waves

that enter the plasma scatter off of particles, in turn accelerating them. The velocity of the particle is related to the difference between the frequency of the initial and scattered wave, as the scattered wave frequency undergoes a Doppler shift. Given their significantly smaller mass, electrons are the particles predominantly accelerated in this process. The signal of the scattered wave, which is typically measured at 90°, has a width that corresponds to T_e and an intensity that corresponds to n_e. AUG has a designated core TS diagnostic and edge TS diagnostic. The edge system has a spatial resolution of 2 mm while the core system has a resolution of 25 mm [27]. The high resolution of the edge system makes the edge TS diagnostic a reliable method of measuring edge T_e and n_e. Both systems have a spatial resolution of 8 ms.

3.4 Profile alignment

The magnetic equilibrium with which ρ_{pol} is assigned is assumed to be toroidally symmetric. The process of mapping measured plasma profiles onto the magnetic equilibrium involves a degree of uncertainty due to geometric concerns such as the spatial resolution of the various diagnostics. To alleviate this uncertainty, profiles measured with different diagnostics can be aligned using small radial shifts.

Studies of power balance and parallel heat transport using heat conduction modeling have determined that for H-mode discharges on AUG the separatrix electron temperature must be approximately 100 eV [28, 29]. This finding can then be used as a marker to align the T_e profile, and an appropriate radial shift is added to obtain 100 eV at the separatrix. The ion temperature profile can then be aligned with the T_e profile such that the position of the steepest gradient for both profiles is the same, an assumption that is valid for plasmas with well-coupled ions and electrons [30]. The uncertainty for this alignment is less than 5 mm.

This H-mode alignment process was performed using LFS measurements profiles.

The HFS profiles that are of interest in this master thesis are then aligned to the LFS profiles. In this case, alignment between LFS and HFS profiles was done using v_{pol} profiles, with the resulting shift then applied to the HFS T_i and intensity profiles. For L-mode and I-mode, the assumption of the electron temperature being 100 eV at the separatrix is not satisfied, and thus the T_e-T_i alignment step cannot be performed. Instead, the L-mode and I-mode radial shifts are based on alignment between LFS and HFS profiles.

3.5 ELM synchronization

For measurements taken of plasmas in the H-mode regime, ELMs complicate the resulting data as they cause cyclical collapses in the temperature and density of the pedestal region. To better characterize the pedestal region, it is necessary to subtract the effect of the ELMs. This can be done using an ELM synchronization technique that relies on using the divertor current to identify the occurrences of ELMs. Given that ELMs are cyclical occurrences, between ELMs the plasma reverts to the conditions it was in before the ELMs, thus subtracting the ELMs results in a steadier profile that appropriately characterizes the plasma during its stable phases. When extracting ELMs from the data, a peak in the divertor current is identified as corresponding to the beginning of an ELM. From this point, the data taken 4 ms after and from 4.5 ms to 1 ms before the next ELM is considered to be useful data. This results in 3.5 ms windows of usable data between ELMs, assuming the ELM frequency is low enough that a window of such length can occur in accordance with the ELM exclusion requirements. For I-mode and L-mode shots, this process is unnecessary as those regimes are characterized by an absence of ELMs.

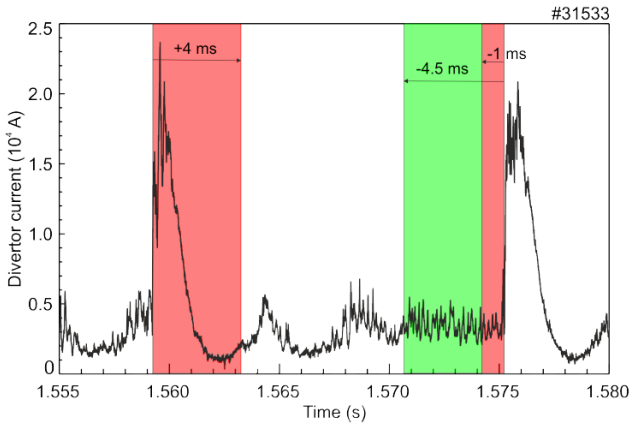

Figure 12: The method of using the divertor current to identify and exclude ELMs from data sets is illustrated above. The red regions of the plot are removed, while the green regions are used to create the pre-ELM profile. Taken from [31]

4 Analysis Tools

4.1 CXSFIT

The complexity of the spectra detected in CX measurements requires fitting routines to appropriately fit and interpret the spectra, extracting the relevant ion data. In this thesis, the code CXSFIT [32] is used to analyze the impurity emissions at the separatrix, the edge of the confined region, and the SOL. When interpreting CX emissions, it must be taken into account that the complex spectra are composed of a superposition of a passive and active spectrum. The passive spectrum is created by emissions from broad-band continuum radiation, thermal neutral charge exchange, and low ionized particles near the plasma boundary, while the active spectrum is produced by the charge exchange reactions between the injected neutrals and the fully ionized atoms that are of interest in CX measurements. Generally, the passive spectrum has a lower intensity than the active spectrum in hot plasmas of several keV, with the strongest passive emissions occurring at the edge of the plasma. The contribution of the active spectrum should be emitted locally at the intersection between the LOS and the path of the diagnostic neutrals, thus isolating the active spectrum gives localized plasma data. The passive spectrum component is non-local and its contribution integrates along the LOS. CXSFIT utilizes modeling based on input plasma parameters to improve passive spectrum identification. The passive and active spectra can be separated from one another using techniques such as beam modulation. CXSFIT functions as a useful tool to process CXRS data while accounting for both passive and active contributions.

CXSFIT is a platform that performs complex Gaussian fitting, with the capacity to design fits that consider multiple emission features at once. In addition to separating the passive emission contributions, CXSFIT allows for the selection of multiple lines

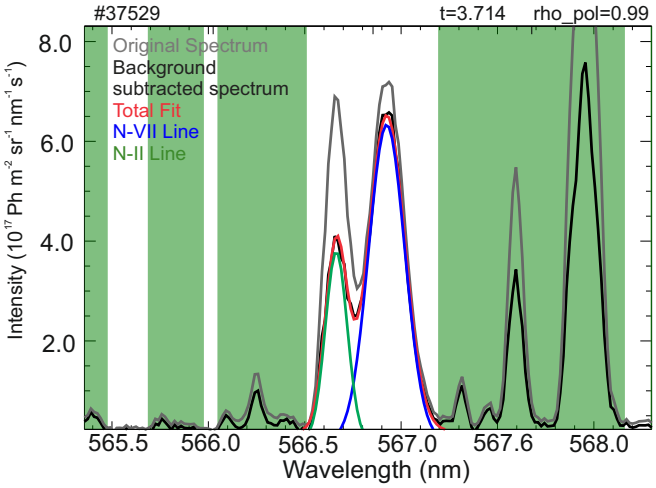

Figure 13: Example of a Nitrogen VII emission fit obtained with CXSFIT. The passive spectrum is represented in gray and ignored in the fit. The active spectrum is represented in black, with the corresponding fit represented in blue. N-VII emission line (566.937 nm) is very close to the N-II (566.663 nm), so a multi-gaussian fit is utilized to separate the contributions of both emissions. Green regions represent spectrum portions ignored in the fit.

and the assignment of prescriptive line value estimates for a more accurate final fit (Figure 13). Through this method, the various line contributions within the composite spectrum can be isolated, resulting in more accurate processing of the individual lines. Using this tool, a multigaussian fit was created to account for the molecular line contamination discussed in section 4.1.1. After fitting the spectra of a discharge, CXSFIT is capable of extracting the temperature, rotation, and intensity of the ions being studied.

4.1.1 Molecular Line Contamination Subtraction

When molecules are used as the injected neutrals for CXRS measurements, as is the case for the gas-puff CXRS diagnostic at AUG used in this work, the molecule will produce its own emission lines that can potentially contaminate the impurity line. The dissociation energy of molecular neutrals is very low, about 3 eV. Given that confined plasmas can reach temperatures of up to a few keV, neutral molecules very

quickly ionize upon entering the plasma, with some regions of the plasma ionizing completely. Within the high temperature plasma, the quantity of neutral molecules is very small, causing their emissions to be significantly less than the impurity emissions and thus negligible in the fitting routine. However, in the scrape-off layer and near the separatrix where the molecular neutral density is greater, the impurity signal is more likely to experience contamination from the molecular emissions. Considering that the GP-CXRS system on AUG injects D_2 and measures at the edge of the plasma, it is crucial to develop a reliable method to subtract away the contamination of the molecular emissions from the impurity spectral line so as to produce accurate edge and SOL profiles.

For this thesis, a multigaussian fit was created using the molecular database in [33] where tens of thousands of spectral lines have been identified for D_2 spanning a large range of wavelengths. The fit was designed by selecting the molecular lines within the range of the theoretical wavelength of the two impurities of interest, nitrogen VII (566.937 nm) and boron V (494.467 nm), to be fitted to their own gaussian. The final fit recipes accounted for 8 molecular lines in the nitrogen fit and 6 molecular lines in the boron fit. Constraints were put on the molecular line contributions such that they all must have the same velocity and temperature, and that the intensity relation between them corresponds to the relative intensity of each line as given in the molecular database [33]. The preliminary estimations for temperature and velocity of the molecular contributions were also selected to be much smaller than the impurity contribution.

4.2 Kinetic Transport Algorithm KN1D

In order to verify whether differences between profiles generated using single- vs multi-gaussian fits are due to molecular line contamination, the kinetic transport algorithm

KN1D was employed to estimate molecular contributions to CXRS measurements. KN1D was created to calculate the neutral atomic and molecular hydrogen distribution functions for specified plasma parameters in a simple, slab-like geometry [34].

One important input parameter for the simulation is the molecular neutral pressure at the tokamak wall. This parameter is derived from the gas flow rate of the gas puff device utilized in the CXRS diagnostic [35] through the equation:

$$P = \frac{1}{4} \frac{u_{D_2} \cdot k_B T}{A_{eff} \cdot \overline{v} \cdot 0.1333} \tag{15}$$

where P is the pressure in mTorr, u_{D_2} is the gas flow rate in particles/s, k_B is the Boltzmann constant, T is the temperature of the neutral gas, $\overline{v}$ is the average molecular velocity, 0.1333 is a conversion factor in $Jm^{-3}/mTorr$, and A_{eff} is the effective area of the gas puff cloud. Another relevant input parameter for the simulation is a one dimensional geometry, shown in Figure 14. This geometry consists of a molecular neutral source, the tokamak wall, the limiter shadow, the scrape-off layer, and the plasma core.

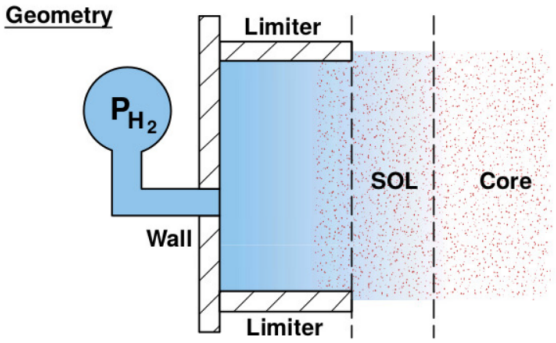

Figure 14: Geometry utilized in KN1D simulation

Lastly, the input requires plasma parameters, specifically the electron density profile, and the ion and electron temperature profiles. For these simulations, profiles fit to experimental data from the H-mode, I-mode, and L-mode discharges were employed

to best approximate experimental conditions.

After inputting plasma parameters, the 1D geometry, and molecular neutral pressure at the tokamak wall, the algorithm proceeds to simulate the plasma-neutral interactions that are typical in divertor tokamaks, such as charge exchange collisions, elastic collisions, and ionization processes. Using this algorithm, the distribution of molecular and atomic deuterium around the separatrix and in the SOL can be modeled for plasmas in different confinement modes. By modelling the density of the neutrals in various plasma conditions, we can evaluate what regions of the plasma are most likely to have impurity profiles impacted by molecular contributions.

5 Results

Ion temperature plays a key role in generating the self-sustaining fusion reaction necessary for a successful fusion reactor, thus it is important to be able to accurately characterize ion temperature throughout the plasma. In the edge and SOL region of the plasma, CXRS ion temperature measurements are potentially complicated by the spectral emissions of the molecular neutrals injected into the plasma to induce CX reactions. To produce more reliable temperature measurements and to evaluate regions most impacted by molecular lines, temperature and intensity profiles are obtained using multi-gaussian fits that account for molecular contributions. The results obtained for this master thesis are outlined in this section.

5.1 Eliminating Molecular Contribution

The presence of molecular contributions to CXRS measurements was identified by comparing plasma profiles developed from a multi-gaussian fit to profiles extracted from a single-gaussian fit. Inside of the separatrix, the profiles show very little difference between the single- and multi-gaussian fits for L-, I-, and H-modes, suggesting the molecular contributions in the confined region of the plasma are minimal for all modes. Outside of the separatrix, all modes showed a decrease in signal intensity when molecular contributions had been substracted away via multi-gaussian fit. Temperature profiles outside the separatrix were reduced by a multi-gaussian fit for the H-mode case, but showed little difference between fits for the L-mode and I-mode cases.

5.1.1 Molecular Contribution in CXSFIT multi-gaussian fit

Figures 15 and 16 feature fitted spectra from L-mode boron V emissions and H-mode nitrogen VII emissions respectively, with the total multi-gaussian fit developed

in CXSFIT shown in red, the D_2 fit components shown in magenta, and impurity line fit component shown in blue. Looking at the overall fit, this multi-gaussian fitting routine is capable of reproducing the experimental spectra while identifying the molecular contributions. Comparing the confined region spectra (Figures 15a and 16a) to the SOL spectra (Figures 15b and 16b) suggests a much larger molecular contribution in the SOL. The confined region spectra are seemingly described using a single-gaussian, indicating an absence of molecular contribution. In the SOL, the molecular emissions are clearly identifiable as the fit becomes a composite of multiple gaussian contributions. This aligns with expected behavior [1], as the low dissociation energy of the neutral molecules would indicate that within the high temperature core the neutrals will have ionized, ceasing their complex emissions.

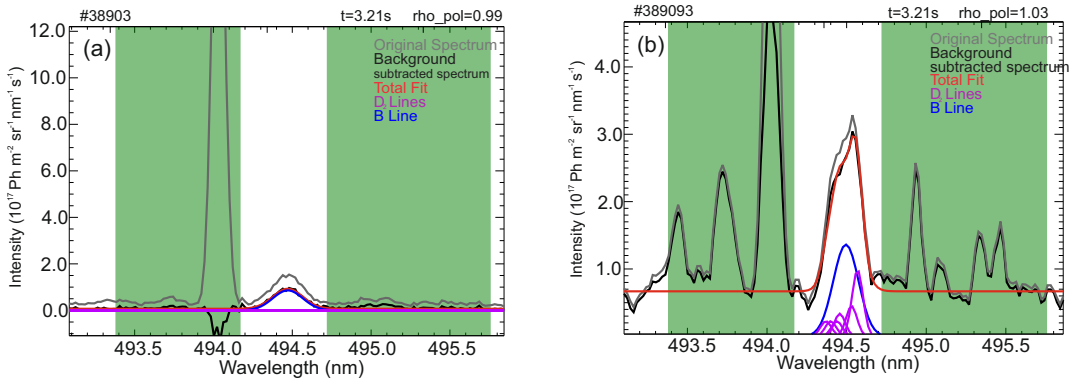

(a) Confined region boron spectrum (b) SOL boron spectrum

Figure 15: CXSFIT multi-gaussian fit for boron spectra measured inside and outside of the separatrix ($\rho_{pol} = 1$) for an L-mode plasma. The boron line is shown in blue, while the molecular emission contributions to the fit are shown in magenta.

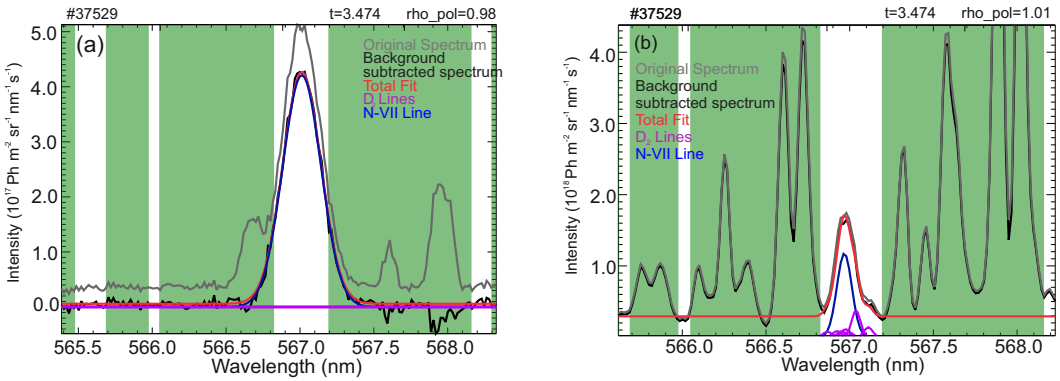

(a) Confined region nitrogen spectrum

(b) SOL nitrogen spectrum

Figure 16: CXSFIT multi-gaussian fit for nitrogen spectra measured inside and outside of the separatrix ($\rho_{pol} = 1$) for an H-mode plasma. The nitrogen line is shown in blue, while the molecular emission contributions to the fit are shown in magenta.

5.1.2 H-mode profile evaluation

The H-mode discharge (#37529) had a toroidal magnetic field of 2.5 T and a plasma current of 1 MA. Both ECRH and NBI heating systems were utilized, with ECRH power injecting 1.35 MW and NBI power injecting 4.8 MW. For the time frames analyzed in this master thesis, the density at the edge of the plasma was $5 \times 10^{19}\ m^{-2}$ and the gas-puff flow rate for the GP-CXRS system was $2.65 \times 10^{21}\ D_2$/second.

Figures 17 and 18 show the intensity and temperature profiles, respectively, for an H-mode plasma measured using the poloidal and toroidal gas-puff diagnostics at the HFS (as introduced in chapter 3.2). Each compares the profiles produced from single- vs multi-gaussian spectra fitting. While all four plots show close alignment between single- and multi-gaussian profiles for the region inside the separatrix, there is disagreement in the SOL, indicating at least partial subtraction of the molecular contributions.

Observing the intensity profile, the diagnostics produce profiles that can be described by a single-gaussian up to about $\rho_{pol} = 1.015$ in the poloidal case (Fig. 17a), and $\rho_{pol} = 1.01$ in the toroidal case (Fig. 17b), indicating the molecular deuterium

neutral has fully ionized well before the separatrix. In the process of subtracting molecular emission contributions, the poloidal diagnostic sees a greater intensity decrease in the SOL than the toroidal diagnostic. This is due to the geometry of the CXRS diagnostics, illustrated previously in Figure 11 from chapter 3.2. The sight lines of the poloidal diagnostic have a larger path through the SOL as compared to the toroidal diagnostic. Given that the molecules are mostly confined to the SOL, the poloidal view sees more molecules than the toroidal view. Accordingly, it is expected that the poloidal diagnostic detects a higher intensity molecular line signal and will see a greater difference between a single- and multi-gaussian fit.

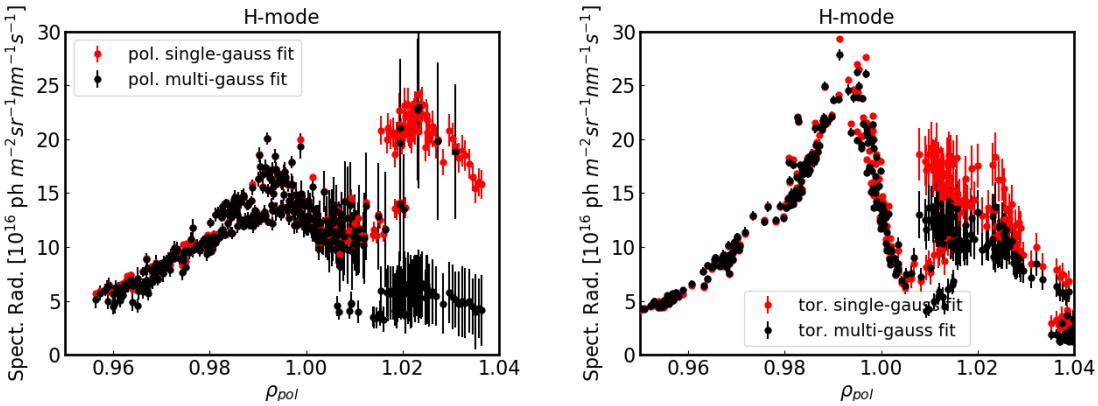

(a) Profiles measured with poloidal optical head

(b) Profiles measured with toroidal optical head

Figure 17: Comparison of H-mode intensity profiles obtained using single-gaussian (red) and multi-gaussian (black) fitting routines

From the intensity profiles, it can thus be expected that the temperature profiles would also show agreement until $\rho_{pol} = 1.015$ with discrepancies at higher ρ_{pol}. For both the poloidal (Fig. 18a) and toroidal (Fig. 18b) temperature profiles, there is indeed agreement until $\rho_{pol} = 1.015$, however any differences in the SOL are very minor in the toroidal view due to the lower molecular line intensity.

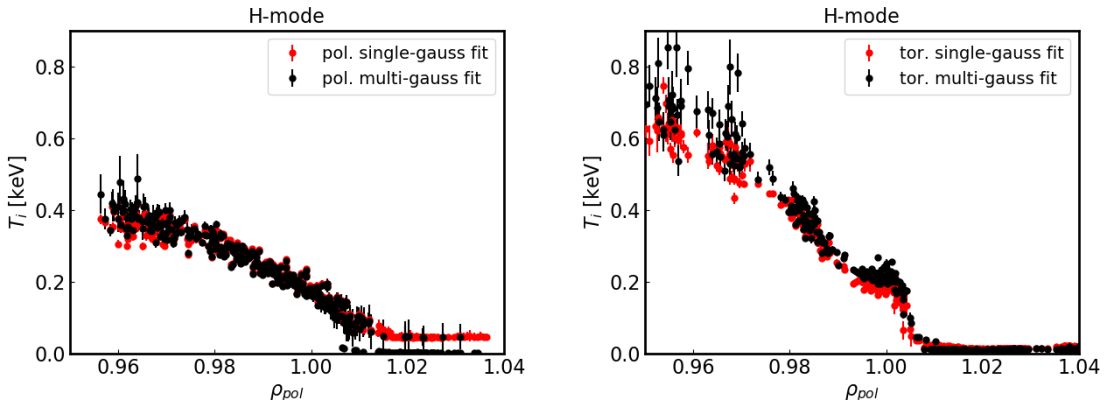

(a) Profiles measured with poloidal optical head

(b) Profiles measured with toroidal optical head

Figure 18: Comparison of H-mode impurity temperature profiles obtained using single-gaussian (red) and multi-gaussian (black) fitting routines

The profiles derived from the two different viewing diagnostics can be compared to evaluate the precision of the ion temperature measurements. The intensity profile diagnostic comparison is shown in Figure 19 and the temperature profile diagnostic comparison is shown in Figure 20.

There is disagreement in the intensity profiles for both single- and multi-gaussian fits. This is to be expected, as intensity is related to the particle density along the path of the LOS for the diagnostic, thus two diagnostics with different LOS will have different intensity. Both diagnostics do undergo a decrease in intensity after the subtraction of molecular line contributions. The intensity measurement can be used to calculate the more informative profile, the impurity density, using the equation:

$$n_Z = \frac{4\pi}{h\nu} \frac{L_{CX,z,\lambda}}{\sum_n \int_{LOS} n_{D,n}(s) \langle \sigma_{n,Z,\lambda} v_j \rangle_{eff}(s) ds} \tag{16}$$

where n_Z is the impurity density, $L_{CX,z,\lambda}$ is the intensity related experimental emissivity of the spectral line, $n_{D,n}(s)$ is the neutral density, $h\nu$ is the photon energy, $\langle \sigma_{n,Z\lambda} \rangle_{eff}$ is the effective CX emission rate, and v_j is the collision velocity. While the

intensity profiles do not need to match between the poloidal and toroidal diagnostics, the measured impurity density should match, and thus the ratio of the intensity to the neutral density along the LOS should be the same. Further data processing would be necessary to evaluate if both diagnostics produce similar impurity density profiles.

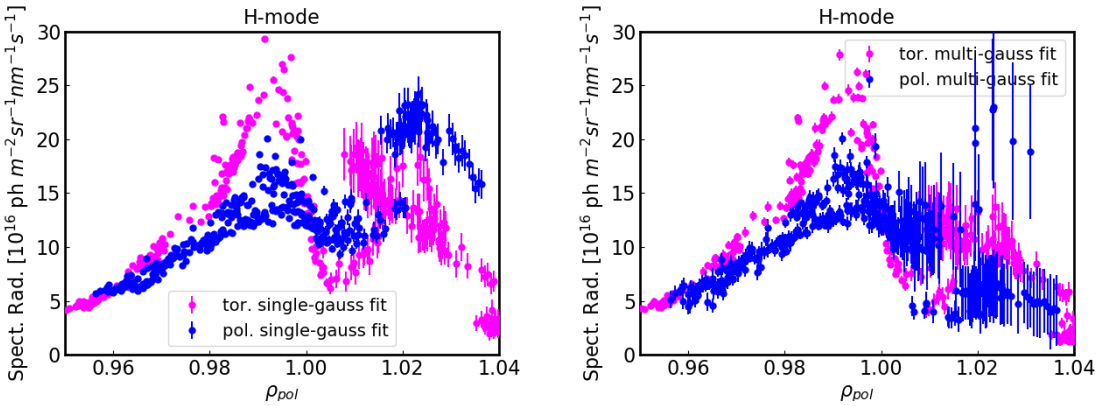

(a) Profiles obtained with single-gaussian fitting routine

(b) Profiles obtained with multi-gaussian fitting routine

Figure 19: H-mode intensity profile comparison for data measured with the poloidal CXRS diagnostic (blue) and the toroidal CXRS diagnostic (magenta)

The temperature profile shows best agreement in the multi-gaussian fit (Figure 20b) in the region between $\rho_{pol} = 0.99$ and the wall at $\rho_{pol} = 1.04$. The two diagnostics diverge in the core for ρ_{pol} lower than 0.99. This is likely due to the difference in diagnostic resolution capability between the poloidal and toroidal diagnostics, discussed briefly in Chapter 3.2. While the toroidal diagnostic maintains consistent resolution for all LOS, the poloidal diagnostic resolution varies across the LOS, becoming worse closer to the core [1]. As the toroidal and poloidal temperature profiles diverge in the enclosed region of the plasma, the higher resolution of the toroidal diagnostic suggests that this measurement is more reliable than the poloidal measurement.

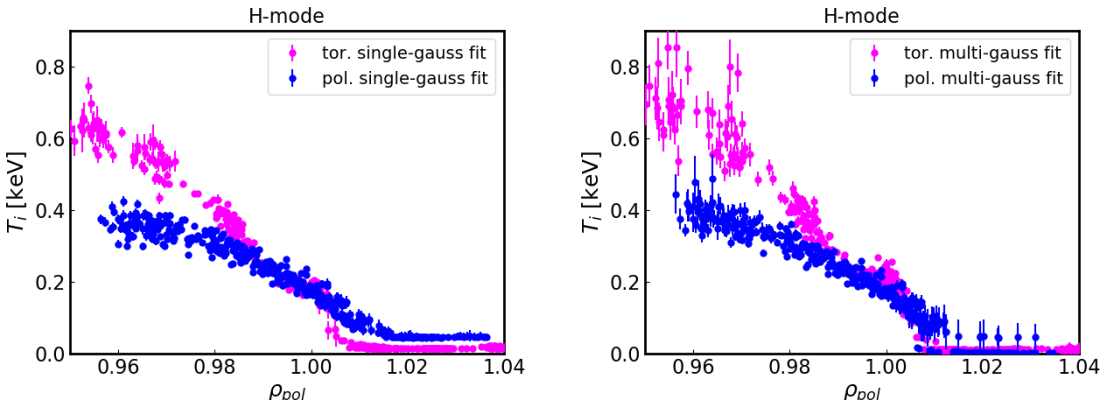

(a) Profiles obtained with single-gaussian fitting routine

(b) Profiles obtained with multi-gaussian fitting routine

Figure 20: H-mode impurity temperature profile comparison for data measured with the poloidal CXRS diagnostic (blue) and the toroidal CXRS diagnostic (magenta)

5.1.3 L-mode profile evaluation

The L-mode discharge (#38903) had the same toroidal magnetic field and plasma current as the H-mode discharge, with $B_t = 2.5$ T and $I_p = 1.0$ MA **CHECK UNIT**. For the time frames analyzed in this master thesis, only the NBI heating system was implemented, with a power of 4.8 MW. The density at the edge of the plasma was $2.7 \times 10^{19}\ m^{-2}$ and the gas-puff flow rate for the GP-CXRS system was $4.0 \times 10^{20}\ D_2$/second.

Similar to the H-mode profiles, both the intensity (Fig. 21) and temperature (Fig. 22) profiles show close agreement inside of the separatrix, indicating full neutral ionization in the core of the plasma. In the SOL, both poloidal (Fig. 21a) and toroidal (Fig. 21b) intensity profiles begin to diverge around $\rho_{pol} = 1.005 - 1.01$, indicating the molecular neutrals penetrate farther for the L-mode case than in the H-mode case. The poloidal diagnostic once again shows a larger intensity in the SOL before subtracting molecular contributions due to the path of the poloidal LOS seeing more molecules. This results in a large reduction from the single- to multi-gaussian fit.

Notably, the intensity of the L-mode signal is much lower than the H-mode intensity by up to a magnitude in some regions. The low intensity results in a noisy signal, which makes complex fitting more challenging.

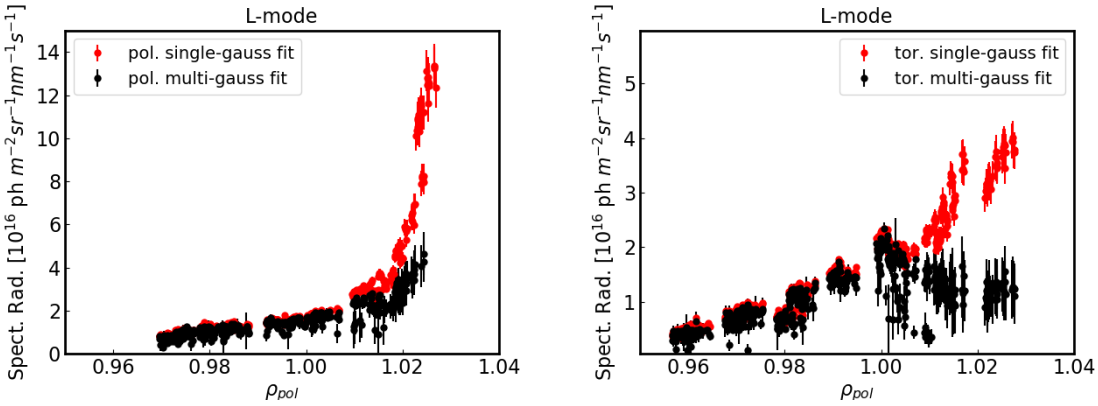

(a) Profiles measured with poloidal optical head

(b) Profiles measured with toroidal optical head

Figure 21: Comparison of L-mode intensity profiles obtained using single-gaussian (red) and multi-gaussian (black) fitting routines

Although the change in intensity profiles in the SOL indicate there is likely molecular line contributions to the detected spectra, the temperature profile does not show much difference between the profile generated from the single-gaussian fit versus that generated from the multi-gaussian fit. This is possibly due to the difficulty of fitting a low intensity signal, which impacts the precision of both fit types. It could also indicate a smaller molecular neutral density in the L-mode discharge. The gas-puff flow rate for this discharge was a magnitude smaller than that of the H-mode discharge, suggesting that there are fewer neutral molecules present to affect the temperature measurement.

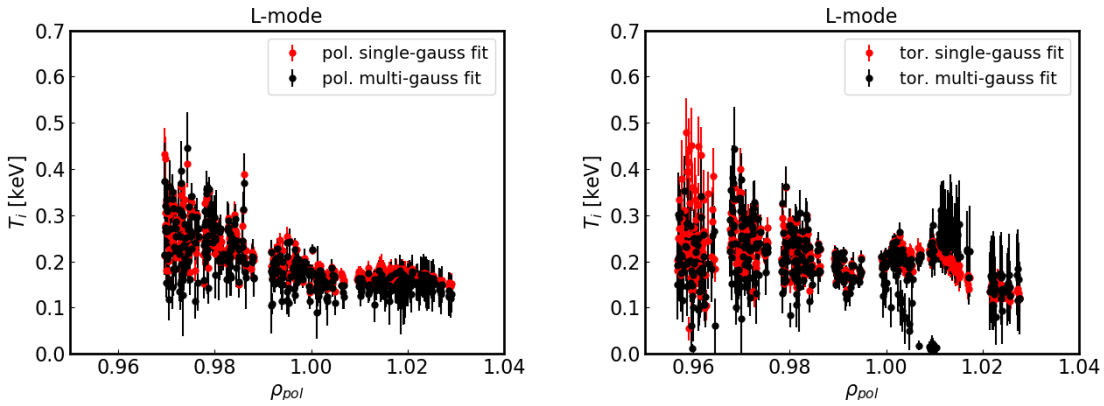

(a) Profiles measured with poloidal optical head

(b) Profiles measured with toroidal optical head

Figure 22: Comparison of L-mode impurity temperature profiles obtained using single-gaussian (red) and multi-gaussian (black) fitting routines

The comparison of the poloidal and toroidal diagnostic profiles for intensity and temperature measurements are shown in Figures 23 and 24 respectively. Until approximately $\rho_{pol} = 1.02$, the profiles match well for both intensity and temperature. Beyond this point, the intensity measurements obtained with the toroidal and poloidal optical heads begin to diverge. Although the poloidal diagnostic is expected to produce greater intensity measurements than the toroidal diagnostic in the SOL due to the fact that its LOS sees more molecular emissions (discussed in the H-mode profile evaluation), this difference in intensity should be largely eliminated by subtracting away the molecular neutral contributions. However, there remains a distinct difference between the two diagnostics even in the multi-gauss fit. This difference suggests the measurements made for $\rho_{pol} > 1.02$ may be unreliable. The temperature profiles show reasonable agreement throughout for both fit types, however they show a larger spread than the H-mode temperature profile, as may be attributed to the lower intensity of the spectra. There is a slight temperature disagreement in the region around $\rho_{pol} = 1.015$ in the multi-gaussian profile. Notably, this radial location corresponds to

the region of lowest intensity for the multi-gaussian fit, suggesting the disagreement may stem from the difficulty of fitting a complex fit to a weak signal

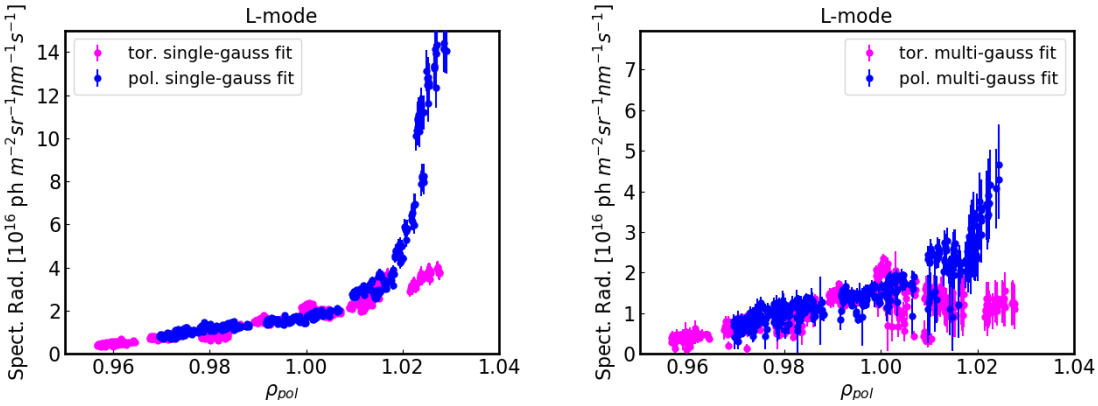

(a) Profiles obtained with single-gaussian fitting routine

(b) Profiles obtained with multi-gaussian fitting routine

Figure 23: L-mode intensity profile comparison for data measured with the poloidal CXRS diagnostic (blue) and the toroidal CXRS diagnostic (magenta)

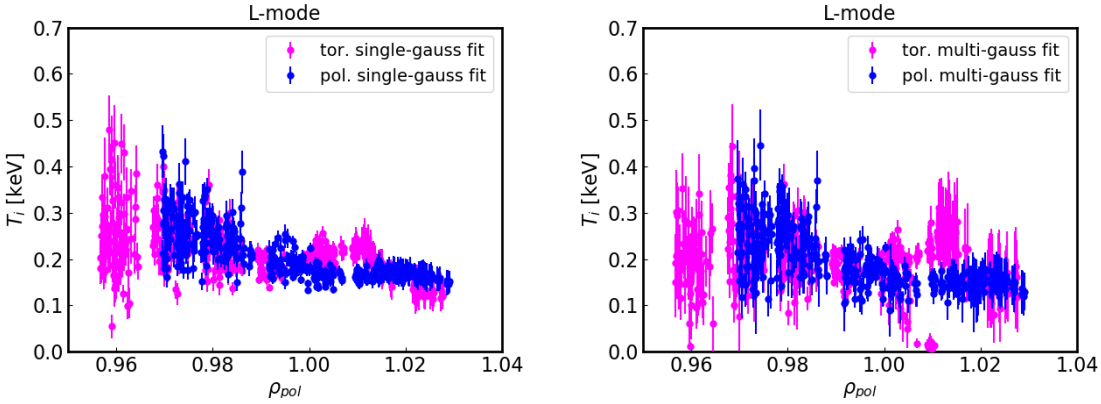

(a) Profiles obtained with single-gaussian fitting routine

(b) Profiles obtained with multi-gaussian fitting routine

Figure 24: L-mode impurity temperature profile comparison for data measured with the poloidal CXRS diagnostic (blue) and the toroidal CXRS diagnostic (magenta)

5.1.4 I-mode profile evaluation

The I-mode discharge (#38905) also had the same toroidal magnetic field and plasma current as the H-mode discharge, with $B_t = 2.5$ T and $I_p = 1.0$ MA. For the time

frames analyzed in this master thesis, ECRH was not used. The NBI system was modulated between 2.0 and 3.0 MW so as to maintain a high temperature without the plasma entering into H-mode. The density at the edge of the plasma was 3.5×10^{19} m^{-2} and the gas-puff flow rate for the GP-CXRS system was 4.0×10^{20} D_2/second.

The single- and multi-gaussian fitted intensity and temperature profiles for the I-mode plasma discharge are shown in Figures 25 and 26. Just as in the H-mode and L-mode case, the fits are approximately the same within the confined region of the plasma, indicating the molecular neutrals have fully ionized before penetrating the plasma. Similar to the L-mode case, the intensity profile begins to diverge at $\rho_{pol} = 1.005 - 1.01$, indicating the molecule in the I-mode case also penetrates farther than the H-mode case. The I-mode profiles display low intensities for both the toroidal and poloidal diagnostics similar to the L-mode case.

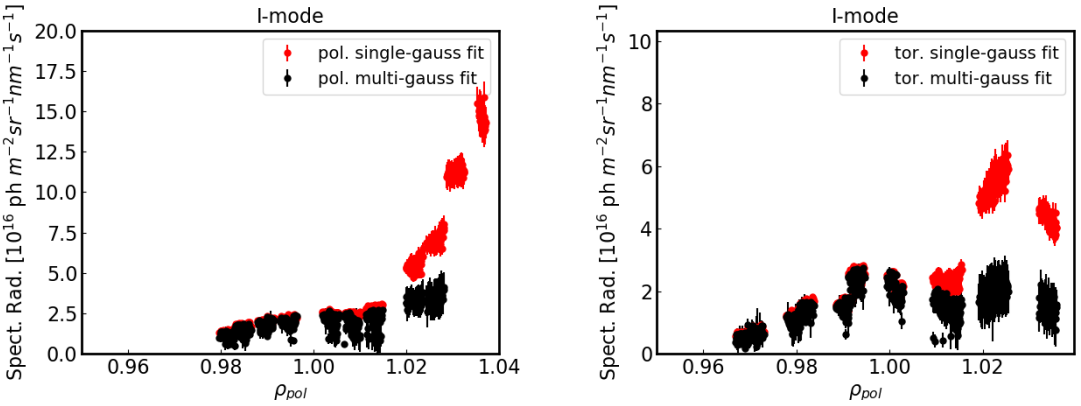

(a) Profiles measured with poloidal optical head

(b) Profiles measured with toroidal optical head

Figure 25: Comparison of I-mode intensity profiles obtained using single-gaussian (red) and multi-gaussian (black) fitting routines

The temperature profiles, much like the L-mode case, align throughout despite the evidence of molecular neutral contributions at higher ρ_{pol}, possibly due to the low signal intensity and the smaller gas-puff flow rate. The I-mode temperatures seem

to be similar to but slightly higher than the L-mode case. I-mode differentiates itself from L-mode by developing a pedestal structure in the temperature profile, however a defined pedestal is not evident in this profile. While the degree of definition of the pedestal can vary depending on the strength of the I-mode, it is possible improved measurements would be necessary to properly distinguish the I-mode pedestal.

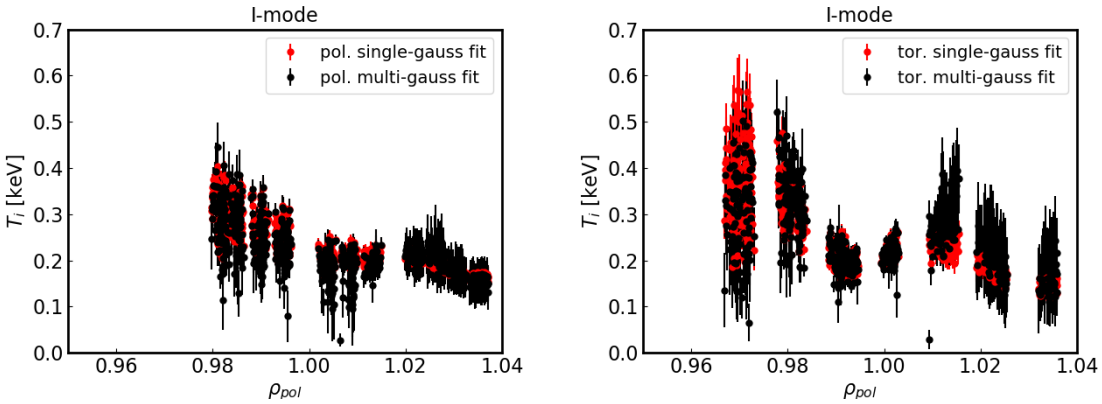

(a) profiles measured with poloidal optical head

(b) Profiles measured with toroidal opticla head

Figure 26: Comparison of I-mode impurity temperature profiles obtained using single-gaussian (red) and multi-gaussian (black) fitting routines

The comparison between toroidal and poloidal measurements can be found for intensity in Figure 27 and for temperature in Figure 28. The intensity profiles match closely up until $\rho_{pol} = 1.03$ for the single-gaussian fit and $\rho_{pol} = 1.02$ for the multi-gaussian fit before diverging similarly to the L-mode case. Thus the measurements made at $\rho_{pol} > 1.02$ may be unreliable for I-mode as well. The temperature profiles show good agreement throughout for both single- and multi-gaussian fits, except for the region around $\rho_{pol} = 1.015$ in the multi-gaussian profile. Like the L-mode case, this radial location corresponds to the region of lowest intensity for the multi-gaussian fit, suggesting the disagreement may stem from the difficulty of fitting a complex fit to a weak signal.

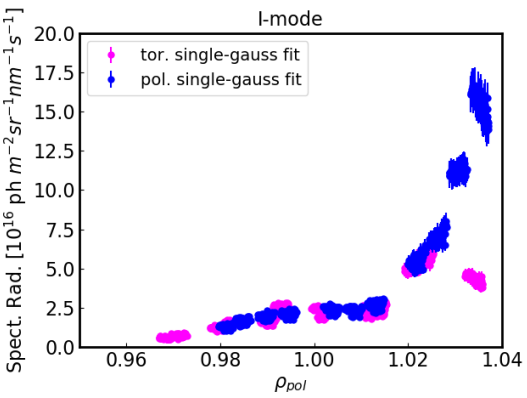

(a) Profiles obtained with single-gaussian fitting routine

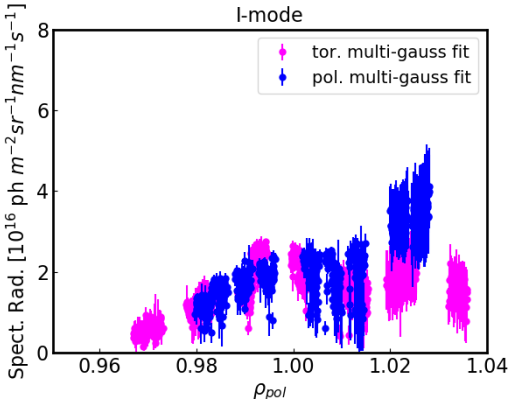

(b) Profiles obtained with multi-gaussian fitting routine

Figure 27: I-mode intensity profile comparison for data measured with the poloidal CXRS diagnostic (blue) and the toroidal CXRS diagnostic (magenta)

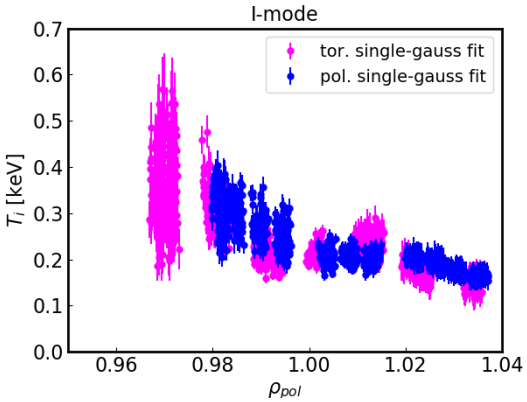

(a) Profiles obtained with single-gaussian fitting routine

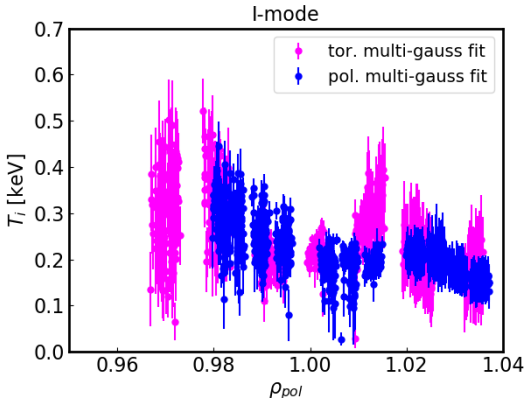

(b) Profiles obtained with multi-gaussian fitting routine

Figure 28: I-mode impurity temperature profile comparison for data measured with the poloidal CXRS diagnostic (blue) and the toroidal CXRS diagnostic (magenta)

5.2 Molecular Hydrogen Modelling using KN1D

Prior work has used KN1D simulations to model the molecular and atomic neutral density distribution in H-mode plasmas, finding that the molecular neutrals do not penetrate beyond about $\rho_{pol} = 1.005$ [36].This finding was reached using input parameters drawn from the experimental conditions of the same H-mode experiment

analyzed in this master thesis. To supplement this finding, this work adjusted the simulation to model L-mode and I-mode plasmas by using input parameters derived from the L-mode and I-mode experiments used in this master thesis. The resulting molecular and atomic D_2 profiles are shown in Figure 29. Considering the L-mode profile (Figure 29a), it appears that the molecular neutrals slightly penetrate the separatrix while the I-mode profile (Figure 29b) shows an abrupt drop around $\rho_{pol} = 1.002$, indicating that beyond that point the molecules are fully ionized. Given that I-mode plasmas maintain higher core and edge temperatures than L-mode plasmas, the degree of neutral molecule penetration produced by these simulations conforms to expectations, with L-mode neutrals penetrating farther before fully ionizing.

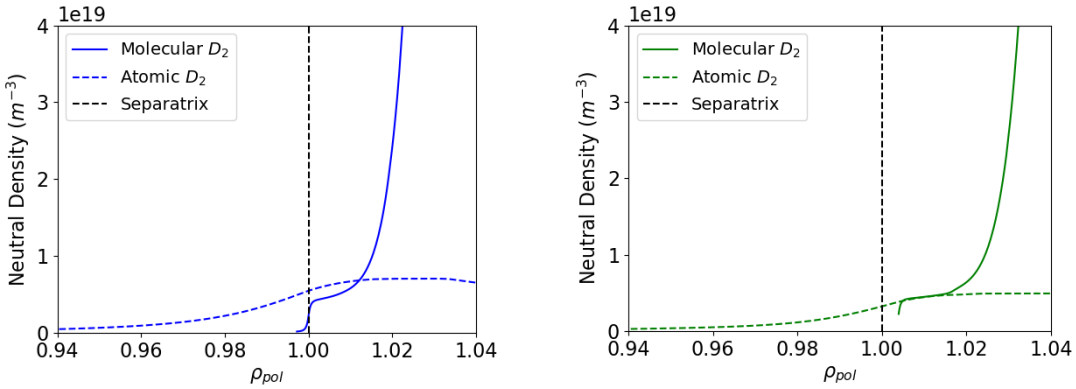

(a) L-mode (b) I-mode

Figure 29: KN1D atomic and molecular neutral density simulation results for L-mode and I-mode plasmas.

In Figure 30, the prior H-mode KN1D results are compared to the L-mode and I-mode results. Similar to the I-mode case, the H-mode molecular density profile undergoes an abrupt decrease outside of the separatrix, indicating that the molecules have undergone full ionization by the time they've reached lower ρ_{pol}. This decrease occurs slightly farther from the separatrix than the I-mode case. These results indicate that molecular neutrals may potentially impact CXRS for the largest range of ρ_{pol},

from just inside the separatrix to the wall. In I-mode, the molecular neutrals may potentially affect measurements for the second largest range, from $\rho_{pol} = 1.005$ to the wall, and in H-mode the molecular neutrals may potentially contribute over the smallest range, from about $\rho_{pol} = 1.007$ to the wall.

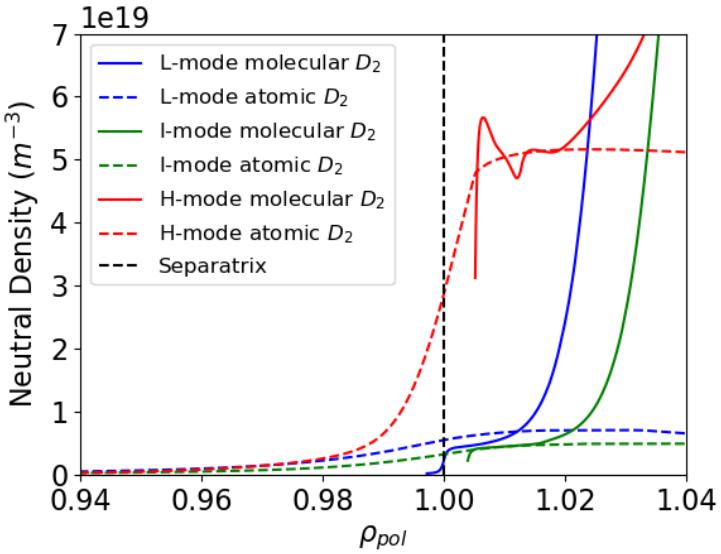

Figure 30: KN1D atomic and molecular density simulation results compared for H-mode [36], I-mode, and L-mode plasmas.

5.2.1 Varied Input Tests

To test the robustness of the modelling results, the L-mode case was run several times varying the input parameters. The prior H-mode KN1D analysis found that varying the ion temperature input profiles negligibly impacted the penetration depth of the molecular neutrals [36], thus these input tests were focused on the electron density and electron temperature input profiles. First, the effect of electron density was tested by keeping all other L-mode simulation inputs constant and testing the output for n_e profiles taken from the L-mode, I-mode, and H-mode experimental parameters. The electron density profiles and the KN1D molecular neutral output are shown in Figure 31. For all three cases, the molecular neutrals penetrate slightly past the separatrix

and fall from their original value at about the same rate, indicating only minimal impact from varying n_e.

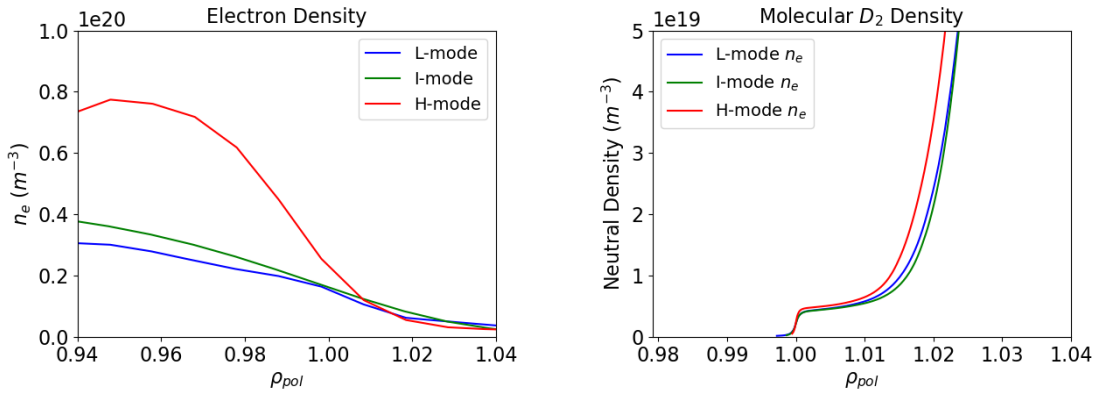

(a) (b)

Figure 31: Varied electron density inputs (Left) result in very similar molecular neutral density KN1D simulation profiles (Right)

This testing method was repeated for the electron temperature, this time keeping the L-mode n_e profile and varying the T_e input profile using the profiles for the three plasma discharges. The input T_e profiles and output molecular D_2 density profiles are shown in Figure 32. The output profiles in this case show much greater sensitivity to the input profile. Only the L-mode T_e case results in a molecular D_2 density profile that penetrates the separatrix, with the I-mode T_e case penetrating the next farthest and H-mode T_e case penetrating the least, much like the profile comparison in Figure 30. This seems to indicate that the ionization process of the molecular neutrals is dependent on the presence of high temperature electrons in the confined region of the plasma. Since the T_e profile becomes similar outside of the separatrix, the electron temperature of the confined region seems to play a much greater role in neutral penetration.

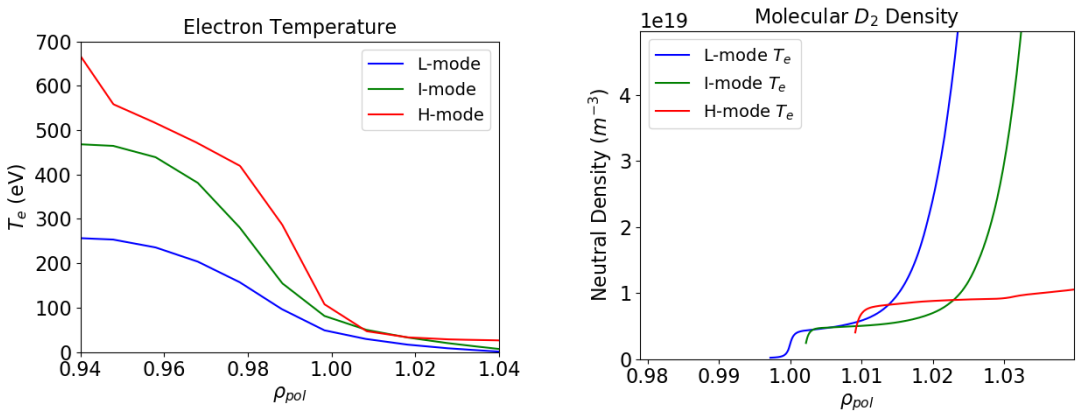

(a) (b)

Figure 32: Varied electron temperature inputs (Left) impact the molecular neutral penetration in KN1D simulation density profiles (Right)

6 Summary and Conclusions

The work presented in this thesis serves to expand upon the diagnostic capabilities of measuring ion temperature at the separatrix and in the Scrape-Off layer in the hopes of contributing to a clearer understanding of this region of the plasma. To do this, Charge Exchange Recombination Spectroscopy (CXRS) impurity data was collected from three different plasma discharges performed at ASDEX Upgrade, representing H-mode, L-mode, and I-mode confinement. In processing the data, this thesis focused on subtracting molecular neutral lines from the detected spectra. The molecular neutrals used by the High Field Side CXRS diagnostics to induce CX reactions emit their own molecular lines which contaminate the impurity line, thus clear characterization of the impurity signal requires elimination of this contamination. To do this, a multi-gaussian fit was designed using CXSFIT to identify the complex contributions to the detected spectra and isolate the impurity line from the molecular lines. Intensity and temperature profiles were generated using single- and multi-gaussian fitting routines to observe the molecular contributions. Then, the profiles obtained from the measurements with the toroidal and poloidal optical heads were compared to identify regions of agreement where temperature measurements can be considered valid.

For all three discharges, there was a distinct difference between single- and multi-gaussian fits in the intensity profile in the SOL. The L-mode and I-mode cases showed molecular contributions starting around $\rho_{pol} = 1.005 - 1.01$, while the H-mode discharge showed molecular contributions starting at $\rho_{pol} = 1.015$. This indicates that the molecular neutrals penetrate farther into the plasma for the L-mode and I-mode conditions before fully ionizing and thus molecular contributions must be considered for a larger range of ρ_{pol}. This seems to suggest that measurements of the temperature at the separatrix ($\rho_{pol} = 1$) are more likely to be effected by molecular lines if

the plasma is in L-mode or I-mode than in H-mode. Subtracting molecular contributions resulted in a decrease in the H-mode temperature profile in the SOL, with the greatest decrease (about 100 eV) noted in the measurements performed with the poloidal optical head. Once molecular line contamination had been subtracted, the H-mode temperature profiles for the poloidal and toroidal optical heads matched well from $\rho_{pol} = 0.99$ to $\rho_{pol} = 1.04$. The disagreement in the enclosed plasma is likely due to poor resolution of some of the innermost poloidal LOS. Subtracting molecular contributions from the L-mode and I-mode spectra did not greatly impact the temperature profiles, possibly due to the low intensity of the signal for these two discharges as compared to H-mode. The difference in intensity between the discharges is likely a result of the difference in flow rate of the gas-puff; the H-mode gas-puff flow rate was a magnitude greater than the flow rates for L- and I-mode. For the I-mode and L-mode temperature profiles, the two diagnostics matched well for the whole profile. However, there was disagreement between diagnostics in the intensity profiles. The poloidal intensity remained high close to the wall even after subtracting molecular line contributions for both the L-mode and I-mode profiles, suggesting that the measurements made between $\rho_{pol} = 1.02$ and $\rho_{pol} = 1.04$ are unreliable for these two discharges.

Finally, the molecular and atomic neutral density was modelled using the 1D kinetic code KN1D. The simulations found that in L-mode, molecular neutrals slightly penetrated the separatrix before being fully ionized. Both I-mode and H-mode molecular D_2 became fully ionized before reaching the separatrix, with I-mode penetrating slightly farther. This is in agreement with experimental findings, as L-mode and I-mode intensity profiles showed molecular contamination closer to the separatrix than the H-mode discharge profiles.

In both the experimental analysis and the KN1D simulation the molecular neutrals

penetrated farther into the plasma in the L-mode and I-mode discharges than the H-mode discharge. However, the experimental temperature profiles for L-mode and I-mode were largely unchanged by subtracting the molecular contributions in the fitting process, while the H-mode case showed a temperature difference in the SOL after the subtraction. The stronger reduction in the H-mode case is because there were significantly more molecules puffed into the plasma for the CXRS measurements. A better comparison between confinement modes would require equal gas flow rate, posing a potential topic for future study. Based on depth of molecule penetration, it appears that impurity temperature measurements at the separatrix are more likely to be affected in L-mode and I-mode discharges, although when CXRS gas-puff flow rates are low, that effect may become negligible. In the H-mode case, the molecular neutrals seem to fully ionize before reaching the separatrix even with a high gas-puff flow rate, suggesting that molecular lines may not need to be accounted for in impurity temperature edge measurements of H-mode discharges. The results presented in this thesis show that multi-gaussian fits can be used to account for molecular line contributions in CXRS measurements, and that these line contributions impact a larger range of ρ_{pol} in L-mode and I-mode discharges than H-mode discharges.

References

[1] D.J. Cruz-Zabala *et al. 3D modelling of diagnostic thermal neutrals to study edge poloidal impurity asymmetries.* Submitted to *Plasma Physics and Controlled Fusion*, 2021.

[2] K. S. Krane, D. Halliday, *et al.m Introductory Nuclear Physics*, vol. 465. Wiley New York, 1988.

[3] EUROFUSION. *European Consortium for the Development of Fusion Energy.* URL http://www.euro-fusion.org/, 2017.

[4] A. Kallenbach. *ASDEX Upgrade description*, EUROfusion, 2016.

[5] JET/EFDA, *Cyclotron*, 1999.

[6] F. Wagner *et al. Physical Review Letters*, 49(19):1408, 1982.

[7] M. Keilhacker *et al. Plasma Physics and Controlled Fusion*, 29(10A):1401–1413, 1987.

[8] E. Viezzer. *Radial electric field studies in the plasma edge of ASDEX Upgrade.* PhD thesis at Ludwig-Maximilians-Universität, Munich, 2012.

[9] A.W. Leonard *et al. Physics of Plasmas*, 21:090501, 2014.

[10] H. Zohm *et al. Plasma Physics and Controlled Fusion*, 38:105–124, 1996.

[11] J.W. Connor *et al. Physics of Plasmas*, 5:2687, 1998.

[12] P.B. Snyder *et al. Physics of Plasmas*, 9:2037, 2002.

[13] D.G. Whyte *et al. Nuclear Fusion*, 50:105005, 2010.

[14] T. Happel *et al., Plasma Physics and Controlled Fusion* 59, 014004, 2017.

[15] J. Rice *et al., Nuclear Fusion*, 55:033014, 2015.

[16] F. Ryter *et al. Nuclear Fusion* 57:016004, 2017.

[17] M. Reith *et al. J. Nuclear Materials*, 432:482, 2013.

[18] Max Plank Institute for Plasma Physics, Online Picture Archive, ASDEX UPGRADE. URL https://www.ipp.mpg.de/1471827/asdexupgrade, 2021.

[19] R.J. Fonck, D.S. Darrow and K.P. Jaehnig, *Physics Review A*, 29:3288, 1984.

[20] R.M. Churchill *et al. Rev. Sci. Instrum.*, 84:093505, 2013.

[21] Max Plank Institute for Plasma Physics, *Neutral beam injection on ASDEX Upgrade and Wendelstein 7-X*, https://www.ipp.mpg.de/3704076/nbiaugw7x, 2021.

[22] E. Viezzer *et al. Plasma Physics and Controlled Fusion*, 55:124037, 2013.

[23] R.M. Churchill, B. Lipschultz and C. Theiler, *Nuclear Fusion*, 53:122002, 2013.

[24] D.J. Cruz-Zabala *et al. JINST*, 14 C11006, 2019.

[25] W. Suttrop. *Practical Limitations to Plasma Edge Electron Temperature Measurements by Radiometry of Electron Cyclotron Emission.* IPP Report 1/306, Max- Planck-Institute for Plasma Physics, Garching, Germany, 1997.

[26] S.K. Rathgeber et al. Plasma Physics and Controlled Fusion, 55:025004, 2013.

[27] B. Kurzan *et al. Review of Scientific Instruments*, 82:103501, 2011.

[28] J. Neuhauser *et al. Plasma Physics and Controlled Fusion*, 44:869, 2002.

[29] A. Kallenbach *et al. Nuclear Fusion*, 43:573, 2003.

[30] P.A. Schneider *et al. Nuclear Fusion*, 53:073039, 2013.

[31] D.J. Cruz Zabala. *Characterization of the ion pedestal in low and high collisionality plasmas*. Master thesis at Universidad de Sevilla, Sevilla, 2017.

[32] A. D. Whiteford, M. G. von Hellermann, L. D. Horton, and K.-D. Zastrow, *CXSFIT User Manuel*. http://www.adas.ac.uk/notes/adasr07-01.pdf.

[33] R.S. Freund, J.A. Schiavone, and H.M. Crosswhite. *J. Phys. Chem. Ref. Data*, 14:235, 1985.

[34] B. Labombard, *KN1D: A 1-D space, 2-D velocity, kinetic transport algorithm for atomic and molecular hydrogen in an ionizing plasma*, tech. rep. PSFC/RR-01-3 (MIT, 2001).

[35] R. Churchill *et al. Review of Scientific Instruments*, vol. 49, no. 9, p. 104014, 2013.

[36] R. López Cansin. *Neutral gas injection for diagnostic purposes in fusion plasmas*. Bachelor thesis at Universidad de Sevilla, Sevilla, 2021.